This is the peer-reviewed, final accepted version for American Mineralogist, published by the Mineralogical Society of America.
The published version is subject to change. Cite as Authors (Year) Title. American Mineralogist, in press.
DOI: https://doi.org/10.2138/am-2021-7690. http://www.minsocam.org/

REVISION 1

High pressure, halogen-bearing melt preserved in ultra-high temperature felsic granulites of the Central Maine Terrane, Connecticut (US)

Silvio Ferrero[1,2], Jay J. Ague[3], Patrick J. O'Brien[1], Bernd Wunder[4], Laurent Remusat[5], Martin A. Ziemann[1], Jennifer Axler[6]

[1] *Universität Potsdam, 14476 Potsdam, Germany*

[2] *Museum für Naturkunde (MfN), Leibniz-Institut für Evolutions-und Biodiversitätsforschung, 10115 Berlin, Germany*

[3] *Yale University, New Haven, CT, 06520-8109, US*

[4] *Helmholtz-Zentrum Potsdam, GFZ, D-14473 Potsdam, Germany*

[5] *Museum National d'Histoire Naturelle, Paris*

[6] *Wellesley College, 106 Central Street – Wellesley, MA 02481*

Abstract

Inclusions of relic high pressure melts provide crucial information on the fate of crustal rocks in the deep roots of orogens during collision and crustal thickening, including at extreme temperature conditions exceeding 1000°C. However, discoveries of high pressure melt inclusions are still a relative rarity among case studies of inclusions in metamorphic minerals. Here we present the results of experimental and microchemical investigations of nanogranitoids in garnets from the felsic granulites of the Central Maine Terrane (Connecticut, US). Their successful experimental re-homogenization at ~2 GPa confirms that they originally were trapped portions of deep melts and makes them the first direct evidence of high pressure during peak metamorphism

and melting for these felsic granulites. The trapped melt has a hydrous, granitic, and peraluminous character typical of crustal melts from metapelites. This melt is higher in mafic components (FeO and MgO) than most of the nanogranitoids investigated previously, likely the result of the extreme melting temperatures – well above 1000°C. This is the first natural evidence of the positive correlation between temperature and mafic character of the melt, a trend previously supported only by experimental evidence. Moreover, it poses a severe *caveat* against the common assumption that partial melts from metasediments at depth are always leucogranitic in composition.

NanoSIMS measurement on re-homogenized inclusions show significant amounts of CO_2, Cl and F. Halogen abundance in the melt is considered to be a proxy for the presence of brines (strongly saline fluids) at depth. Brines are known to shift the melting temperatures of the system toward higher values, and may have been responsible for delaying melt production via biotite dehydration melting until these rocks reached extreme temperatures of more than 1000°C, rather than 800-850°C as commonly observed for these reactions.

Keywords

High pressure granulites, anatexis, nanogranitoids, carbon, halogens, piston cylinder

INTRODUCTION

The investigation of melt inclusions in felsic (Ferrero et al., 2015; Cesare et al., 2015) and mafic (Ferrero et al., 2018a) granulites is the most straightforward approach to the investigation of melting processes in the lower continental crust, directly in their source region. These droplets of anatectic melt are generally partially to totally crystallized, i.e. as nanogranitoids, due to the slow cooling of the host rock (Ferrero et al., 2012; Cesare et al., 2015). They contain a cryptocrystalline aggregate of phases consistent with the crystallization of a silicate rich melt (Ferrero et al., 2018b). The expected phases include, but are not limited to, OH-bearing phases, quartz, and feldspar(s), or their metastable polymorphs (Ferrero et al., 2016b). Just like fluid and mineral inclusions, melt inclusions in metamorphic rocks are tools for natural scientists to peer into the history of the host rocks, obtain geochemical information on deep processes, and to better constrain *P-T-t-X* evolution (Ferrero and Angel, 2018).

Multiphase inclusions with features consistent with nanogranitoids were reported by Axler and Ague (2015) in garnets from layers of sillimanite-rich rocks hosted in gneisses of the Central Maine Terrane (CMT - Acadian orogeny, NE Connecticut, US). Phase assemblages in the inclusions and microstructures classify them as former droplets of melt trapped during garnet formation at the metamorphic peak, ~1050°C and ≥1 GPa (Axler and Ague, 2015). The host rock has attracted considerable interest in recent years because of its very high T of re-equilibration at relatively low P (including cordierite-spinel assemblages), allowing Ague et al. (2013) to interpret them as the first example of ultrahigh temperature (*UHT*) metamorphic rocks in North America. By definition, *UHT* metamorphism involves T in excess of 900°C achieved along apparent geothermal gradient ≥20°C/Km (Brown, 2006), i.e. mostly in the stability field of sillimanite. *UHT* metamorphism has been to date identified in dozens of localities worldwide,

mostly in Precambrian rocks (Kelsey, 2008), although much younger *UHT* rocks, i.e. Miocene in age, have been also recently reported (Pownall et al., 2018). More recent studies of other rocks in the CMT document high-pressure granulite facies metamorphism (~1050 °C, ~1.8 GPa) of silica-undersaturated garnet-spinel-corundum gneisses (Keller and Ague, 2018), as well as UHP metamorphism (Keller and Ague, 2020).

Piston cylinder re-homogenization followed by in situ characterization is a common and well-established approach for nanogranitoids studies to follow in order to (1) prove that they originally were indeed droplets of melt, and (2) characterize geochemistry and fluid content and speciation content of anatectic melt (e.g. Acosta-Vigil et al., 2016; Bartoli et al., 2016; Carvalho et al., 2019; Bartoli et al., 2019). Our detailed experimental and microchemical work confirmed that the CMT multiphase inclusions were originally a hydrous and halogen-rich granitic melt formed at T in excess of 1000°C, the hottest preserved melt so far found in natural metasedimentary protolith. Our approach leads to surprising outcomes with broad significance in terms of melt composition and melting processes in the deepest parts of orogenic root zones, as well as of regional geodynamic evolution.

METHODS

Our study used a piston cylinder press, back-scattered-electron (BSE) imaging, electron probe analyses (EPMA), energy-dispersive-spectrometry (EDS) elemental mapping and micro-Raman spectroscopy. Several garnet chips with unexposed nanogranitoids of both equant and tubular shape were manually separated from doubly-polished thick sections and used as starting material in re-homogenization experiments. The chips were loaded in platinum capsules of 4mm length, 3mm diameter, and cold-sealed after filling. Four or five chips were used per each experiment, depending on the size of the chips. Powdered silica was added in the capsule to isolate the chips

both from each other and from the capsule walls, and no water was added to the experimental charge. The pressure cells consisted of talc-pyrex glass outer sleeves with graphite furnace and crushable alumina inner spacers in which the Pt-capsule was embedded (for more details on the experimental setup see Bartoli et al., 2013a; Cesare et al., 2015; and repository data of Ferrero et al., 2015). The assemblage was then kept in a Johannes-type piston-cylinder apparatus at GFZ-Potsdam at variable T and P conditions for up to 24 hours. The temperature (*T*) in the capsule was controlled using a Type S thermocouple (Pt-PtRh10) with a ±10 °C uncertainty. The assemblage has been pressure calibrated via the equilibrium quartz = coesite according Mirwald and Massonne (1980), which is accurate within 50 MPa. Quenching of the experimental charge took place at high *P*, and the machine was unloaded only after reaching ambient *T*. In-situ analyses were then performed on capsules mounted in epoxy and polished to expose re-homogenized inclusions (for further details see Bartoli et al. 2013a; Ferrero et al. 2015).

The Field Emission Gun electron microprobe (FEG-EMP) JEOL Hyperprobe JXA-8500F available at the Natural History Museum of Berlin was used to acquire high-resolution BSE images and EDS elemental maps on nanogranitoids and re-homogenized inclusions. The glass resulting from re-homogenization was analyzed using a JEOL JXA-8200 EMP at Potsdam University. Analytical conditions were similar to previous studies of nanogranitoids (Ferrero et al. 2012; 2015) at 15 kV, 3.5 nA and beam diameter of 1 μm to avoid contamination from the surrounding host. Alkali loss correction factors were estimated using haplogranitic standards (Morgan and London, 2005) and are in the range 17-23% relative for Na_2O and 10-13 % relative for K_2O depending on the analytical session.

Fluorine, CO_2, and H_2O analyses were performed via Nano Secondary Ion Mass Spectrometry (NanoSIMS) using the Cameca NanoSIMS 50 operated at the Muséum National d'Histoire

Naturelle of Paris following the procedure described in Bartoli et al. (2014) and Créon et al. (2018). Polished capsules with re-homogenized inclusions on the garnet surface were mounted in Indium along with standard glasses, and the inclusions identified through images of $^{28}Si^-$ and $^{56}Fe^{16}O^-$ secondary ions. Pre-sputtering on a 5 × 5 μm^2 surface area for 2 min preceded each analysis in order to remove gold coating, surface contamination and achieve a steady-state sputtering regime (Thomen et al., 2014). A 20 pA Cs^+ primary beam was used for data acquisition via rastering of a 3×3 μm^2 surface area. Ions were exclusively collected from the inner 1×1 μm^2 (using the beam blanking mode) to minimize surface contamination. Each analysis comprised 200 cycles with a duration of 1.024 s. Secondary ions of $^{12}C^-$, $^{16}OH^-$ (proxy for H_2O), $^{19}F^-$, $^{28}Si^-$ and $^{56}Fe^{16}O^-$ were recorded simultaneously in multicollection mode, using electron multipliers with a dead time of 44 ns. Mass resolution was set to 5500 to resolve any mass interference on the selected ions. Only analyses with a stable $^{16}OH^-/^{28}Si^-$ ratio were considered in this study. Three glasses of leucogranitic composition and known concentrations of H_2O, varying between ~0.3 and 4.86 wt.% were used for calibration (Bartoli et al., 2014; see also Supplementary material). For F concentration, we used NIST 610 and 612 standards to determine $[F]/[SiO_2]$ ratios from $^{19}F^-/^{28}Si^-$ (Hauri et al., 2002). Four trachyandesitic standards (STR 9, 10, 11 and 13) were used to correct for carbon measurements (Créon et al., 2018): these are glass fragments of shoshonite lava from the Stromboli volcano that were experimentally doped in carbon and water by Bureau et al. (2003). Analytical uncertainty on each NanoSIMS measurement (based on the Poisson error due to counting statistics) was combined with the uncertainty on the calibration (corresponding to 66% interval of confidence) by quadratic sum to obtain the 66% uncertainty on values reported in Table S1.

Micro-Raman spectroscopy was performed using a HORIBA Jobin Yvon LabRAM HR 800 located at the Institute of Geoscience, University of Potsdam. An air-cooled Nd:YAG laser was used for excitation (λ = 532 nm, laser power on the sample of 2–3 mW) with a grating of 300 lines/mm, slit width and confocal hole set to 100 μm and 200 μm, respectively. The Raman spectra of re-homogenized glass inclusions as well as crystal phases were acquired with a 100× objective in the wavenumber range 100–4000 cm^{-1}, integrating 3 repetitions of 30 s with spectral resolution of 10 cm^{-1}. The Raman map in figure 2 was acquired using a spot diameter of 1–1.5 μm and consists of a grid of 19 × 22 points separated by 0.7 μm. Each spectrum was obtained integrating 2 repetitions of 30 s in 4 spectral windows. The software LabSpec 6.0 was used for spectral processing. The inclusion was mapped at ~5 μm depth, causing the spectra to be superimposed by strong Raman bands of the garnet host. The complete garnet spectrum was removed with adopted peak intensity of the most intense garnet band at each point of the map, in order to improve the visibility of the spectra of the mineral phases. Few points showed luminenscence, which was then removed via background substraction. Different phases were visualized in the map by color coding of the indexed Raman bands of the phases (cf. O'Brien & Ziemann, 2008).

PETROGRAPHIC FEATURES OF THE STARTING MATERIAL

The host rocks are rusty schists characterized by the assemblage garnet+sillimanite+K-feldspar+plagioclase+quartz+cordierite+biotite (Fig.1a). The sillimanite is commonly found as pseudomorphs after kyanite. Detailed information on sample location and petrographic features are in Axler and Ague (2015). The inclusions occur in the inner part of garnet porphyroblasts with a random distribution indicative of a primary nature, i.e. entrapment during growth of the

host garnet (Fig. 1b; see also Ferrero et al., 2012). They vary in shape from isometric with diameter ≤10 μm (Fig. 1c) to needles with length ≤100 μm and few μm across (Fig. 1d). The latter type is by far the most common in each cluster, a shape never before observed in such abundance in case studies of nanogranitoid, which are more commonly isometric (Ferrero et al., 2018b; Cesare et al., 2015). The most elongated inclusions often show cracks of limited extension at the corners, evidence of decrepitation. The detailed microchemical and microstructural investigation of the inclusions performed by Axler and Ague (2015) showed that, before the experimental runs, they contain a rather constant assemblage consisting of quartz, phlogopite, white mica and, very often, a compositionally variable phase (CV phase in Axler and Ague 2015) interpreted as residual glass or its nanocrystalline breakdown product.

Raman investigation (Fig. 2a) and mapping of isometric inclusions shows that cristobalite is present instead of quartz in some inclusions (Fig. 2b) and coexists with two micas and accessory phases such as apatite and ilmenite (Fig. 2c, d, e), whereas no inclusions show the presence of residual glass. However, the Raman map shows a crystalline phase with main peaks at 292, 430 and 479 cm^{-1}, assigned to a still unidentified and possibly new phase (hence "phase 430") already found and analyzed in nanogranitoids from HP/UHP rocks of the Bohemian Massif (unpublished data), and having a composition similar to a granitic glass. Graphite occurs as mineral inclusions in garnet and occasionally as a trapped phase in the inclusions. A prominent feature of the host garnet is the presence of abundant rutile and ilmenite needles dominantly oriented parallel to <111> of garnet. Interestingly, needle-shaped nanogranitoids are oriented in the same directions, and may contain rutile or, very rarely, ilmenite as trapped phases (Axler and Ague, 2015).

RESULTS

Five re-homogenization experiments were performed at T=1050°C and variable confining *P* in the range 1.0 – 2.0 GPa (details on experimental runs and products are in Table 1; P-T conditions of each experiment are summarized in Fig. 3). The experimental conditions were chosen to be as close as possible to the conditions of formation, estimated to be ≈1040°C based on Zr-in-Rt thermometry (Tomkins et al., 2007) on the rutile needles present along with nanogranitoids in the garnet core (Axler and Ague, 2015). The *T* estimates were calculated assuming 1 GPa as formation P of the host garnet and melt entrapment, thus representing a minimum value (Ague et al., 2013).

Each experiment shows complete re-melting of the inclusions, i.e. no leftovers of the original phases in the nanogranitoids are visible after the heating run, with the exception of clearly trapped accessories such as rutile and ilmenite. The absence of embayments and the presence of regular linear walls in the inclusions rules out that garnet dissolved into the melt (Ferrero et al., 2012; Bartoli et al., 2013b), as expected in case of significant overheating during the experiments, i.e. the chosen *T* is likely very close to the liquidus of the trapped melt. However, the experiments performed at P <1.7 GPa (numbers 1, 2 in fig. 3) constantly show formation of new garnet, higher in Mg than the original host phase (Figs. 4a,b,c,d) and occasionally small orthopyroxene crystals identified via Raman spectroscopy at P ≤1.2 GPa. Moreover, at 1 GPa most inclusions show extensive evidence of decrepitation (Fig. 4a). The three experiments performed at 1.7 and 2.0 GPa (numbers 3, 4 and 5, Fig. 3) do show fully re-homogenized glassy inclusions without evidence of decrepitation and/or formation of new phases (Figs. 4e,f,g,h,i).

Melt composition

This is the peer-reviewed, final accepted version for American Mineralogist, published by the Mineralogical Society of America.
The published version is subject to change. Cite as Authors (Year) Title. American Mineralogist, in press.
DOI: https://doi.org/10.2138/am-2021-7690. http://www.minsocam.org/

The glass measured in nineteen inclusions (Table2) after successful experimental re-homogenization is hydrous, granitic (Fig. 5a,b) and very K-rich (av. K_2O/Na_2O= 3.90, Table 2), with a clear peraluminous (ASI=1.22, Fig. 5c) and alkalic to alkali-calcic character (Fig. 5d). Importantly, such melts are not leucogranitic, as commonly expected for anatectic melts from melting of metasediments: they have indeed a rather high FeO+MgO content (4.05 wt.%; 4.25 wt.% when recalculated on an anhydrous basis; Table 2). The presence of H_2O in the glass is visible in Raman spectra acquired on re-homogenized nanogranitoids, which show the broad band of water in the region 3200-3800 cm^{-1} (Fig. 6).

The H_2O content of the melt, along with CO_2 and F, was measured in garnets from experiments #3 and #4 using NanoSIMS. One single inclusion shows very low values of all three volatile species, suggesting that it may have lost most of its volatiles possibly as result of decrepitation during quenching (measurement Exp3_MI_1 in Table 3) and thus it is not further considered in the average values calculated below. The volatiles were quantified as 4.40 wt.% H_2O, 3072 ppm CO_2 and 3161 ppm F on average (Fig.7a). With the exclusion of the single analysis discussed above, H_2O content in the rest of the dataset is rather consistent (Fig. 7a), whereas the CO_2 and F contents of the melt vary by an order of magnitude (Figure 7a; Table 3) depending on the inclusion (Fig. 7b, c). Interestingly, EMP measurements on the re-homogenized inclusions show that Cl is also present in remarkable amounts, reaching almost 1 wt.%, with average 0.32 wt.%, making this melt more enriched in halogens (Cl, F) than any previous anatectic melt so far investigated in nanogranitoids.

DISCUSSION

The present study targets polycrystalline inclusions in garnet form felsic granulites of the Central Maine Terrane. Our results confirm that they are volumes of crystallized melt trapped during garnet growth at the metamorphic peak, as already proposed based on mineralogical and microstructural investigation by Axler and Ague (2015). Raman investigation shows the presence of metastable cristobalite, i.e. formed outside its stability field (see e.g. Hwang et al., 2004). The occurrence of metastable polymorphs in nanogranitoids has been interpreted as direct evidence that the inclusions preserve their original composition, as these phases recrystallize to their most common counterparts (i.e. quartz) when the inclusions decrepitates, i.e. becomes an open system able to exchange components with the rock matrix via cracks in the host garnet (Ferrero et al., 2016b). Such inclusions therefore offer access to unaltered deep melts still preserved in the natural rock which underwent melting at depth (Ferrero and Angel, 2018).

The investigation of CMT nanogranitoids thus provides a detailed portrait of formation conditions, geochemistry, and volatile content of melt from metasediments at crustal depth. The extremely high T at which the melt was produced is rather close to the Bt-out curve according to the melting experiments on metasediments of Auzeanneau et al. (2006). Indeed the peraluminous and granitic nature of the re-homogenized melt, its relatively low amount of H_2O and its occurrence in (peritectic) garnet are all features consistent with melt generated by biotite dehydration melting (Le-Breton and Thompson, 1988), with residual biotite still locally visible as mineral inclusions (Fig. 1a). Furthermore, the enrichment in chlorine and fluorine of the trapped melt is likely to influence the stability of the biotite (see paragraph "volatiles in high pressure melt").

The composition measured in the re-homogenized inclusions, especially its granitic character and the high K/Na ratio (≈4:1) is consistent with the phase assemblage, which always includes

quartz/cristobalite plus two K-bearing phases (muscovite and phlogopite). The phase 430 identified via Raman investigation is likely to be the "phase CV", reported in these inclusions by Axler and Ague (2015): the narrow peaks visible in its Raman spectrum show that it belongs to a crystalline phase. Moreover, very similar compositions to the one reported by Axler and Ague (2015) were measured in phase 430 from garnet pyroxenites from the Granulitgebirge (Bohemian Massif; unpublished EMP data; Ferrero et al., in preparation), thus making this phase the main Na repository in the targeted nanogranitoids. The K-rich character of the melt has been previously observed in other nanogranitoid case studies (Cesare et al., 2009; Ferrero et al. 2012) and appears to be a typical feature of primary anatectic melts from metasediments melted at T ≥900°C (see Gianola et al., 2020 and related references).

A peculiarity of this case study is represented by the shape of the inclusions. Most case studies of nanogranitoids show inclusions with a more or less developed negative crystal shape, the response of host garnet to the need of lowering the surface free energy of the melt-garnet interface and move toward textural equilibration (Ferrero et al., 2012). Tubular/acicular shapes in nanogranitoids are not unheard of (Ferrero et al, 2012; Cesare et al., 2015) but they are overall a rarity. CMT nanogranitoids are a rather unique case as the acicular shape, i.e. defined by an extreme elongation/width ratio which characterizes the majority of the inclusions (Fig. 1b,c). So far only the polycrystalline inclusions in the garnet megacrysts of Gore Mountain in the Adirondacks (Darling et al., 1997) show similar features, although in the latter case only ~50% of the inclusions have such shape (Ferrero and Angel, 2018). Further investigations are needed to understand the reasons underlying the dichotomy negative-crystal versus acicular shape in inclusions from different localities.

The original rationale for our work was two-fold: verifying the former melt nature of the inclusions and obtaining the bulk composition of the original melt. The study however generated three most unexpected results: (a) re-homogenization experiments show that this melt formed under high pressure (*HP*) conditions, in contrast with previous studies of these felsic granulites; (b) although the melt itself is peraluminous and granitic in composition, rather common features in melts from metasediments, it has an unexpectedly high mafic (FeO+MgO) component; and (c) in terms of volatiles, the melt contains significant amounts of halogens (Cl, F) besides typical species observed in silicate melts, e.g. H_2O and CO_2.

First evidence of *HP* in the felsic granulites of the Central Maine Terrane

Possibly the most consequential result of our study is that the inclusions re-homogenize completely in equilibrium with the host garnet only at $P \geq 1.7$ GPa, considerably in excess of the minimum of 1.0 GPa inferred by Ague et al. (2013) and Axler and Ague (2015). Garnet growth conditions and thus MI entrapment coincide with those of partial melting, as both garnet and melt are products of the same melting reaction (Cesare et al., 2015 and references therein), and are under chemical equilibrium during their formation. Thus, successful re-homogenization experiments on nanogranitoids are a completely independent tool to constrain the PT conditions of garnet formation in presence of melt (Ferrero et al., 2018b). Both *P* and *T* still need to be calculated beforehand using independent methods, e.g. thermodynamic modeling and classic geothermobarometry on the metamorphic assemblage to which the inclusion-bearing garnet belongs, in order to proceed with the experiments. If the calculated formation conditions are correct, (most of) the nanogranitoids should re-melt completely without reacting with the host during the experimental run (Bartoli et al. 2013b; Acosta-Vigil et al., 2016;). Conversely, textural

289 evidence of melt-garnet disequilibrium as well as decrepitation evidence would indicate the
290 experimental parameters were not representative of the formation conditions (Ferrero et al.,
291 2018b; Ferri et al., 2020; Gianola et al., 2020). As an example, the critical evaluation of the
292 nanogranitoid microstructures after heating experiments at different P allowed Ferrero et al.
293 (2018b) to bracket the P conditions of melting of the felsic granulites of Orlica–Śnie nik Dome
294 (OSD; Bohemian Massif) to 2.7 ±0.1 GPa, starting from an initial range of calculated *P* spanning
295 from 1.8 to 3.0 GPa based on previous geothermobarometric and modelling studies.

296 Our detailed experimental work on the CMT nanogranitoids shows that the nanogranitoids re-
297 melt at *T*=1050°C. At 1.0 GPa the abundance of decrepitation cracks in the re-melted inclusions
298 is a clear evidence of insufficient confining *P*, which leads to failure of the container (the garnet)
299 due to inclusion overpressurization during the heating run. Moreover, all the experiments at *P*
300 <1.7 GPa show evidence of chemical disequilibrium between the newly produced glass and the
301 surrounding garnet. This causes melt-garnet interaction, with formation of new phases not present
302 in the inclusions before experimental runs, e.g. orthopyroxene and/or change in composition
303 (Mg-increase) of the garnet around the inclusion. Newly formed, Mg-richer garnet was also
304 reported in nanogranitoids from the OSD felsic granulites after experiments at *P* lower than those
305 of melt formation (Ferrero et al., 2018b). Hence the microstructural appearance of the CMT
306 nanogranitoids after reheating show an evolution similar to that reported in Ferrero et al. (2018b),
307 with the Mg-rich garnet disappearing once the confining *P* reaches 1.7 GPa, thus demonstrating
308 that both garnet and melt formed at P ≥1.7 GPa.

309

310 **High mafic content in pristine anatectic melt from metasediments**

311 Granitic melts with geochemistry similar to the CMT nanogranitoids, i.e., high ASI index,
312 rather high normative orthoclase and high FeO+MgO, are reported from experiments on natural
313 metapelitic rocks at 1 GPa and 1025-1075 °C (Patiño-Douce and Johnston, 1991) and in
314 nanogranitoid from metapelitic migmatites which experienced UHT conditions, 950°C and 0.5
315 GPa, in the Kerala Khondalite Belt, Southern India (Cesare et al., 2009; Ferrero et al., 2012; see
316 table 2 and fig. 8a,b for the whole nanogranitoid and experimental dataset). It may be argued that
317 such a mafic-rich character is the result of contamination between glass and host, as the
318 inclusions are hosted in Fe- and Mg-rich garnet (Axler and Ague, 2015). However, contamination
319 via (even limited) dissolution of garnet during re-heating experiments can be excluded based on
320 microstructural basis, i.e. the inclusions show regular shapes and completely lack embayments
321 indicative of garnet dissolution. Contamination during EMP analysis can be also ruled out for the
322 inclusions selected for EMP investigation and reported in Table 2. The size of the re-
323 homogenized inclusions was sufficiently large (>5 μm in diameter) to avoid the excitation
324 volume created by the electron beam (diameter 1 μm) to come in contact with the host. In the few
325 cases where the inclusions were ≤5 μm, garnet contamination was clearly visible as the measured
326 SiO_2 showed a sharp decrease, coupled with FeO increase (Fig. 8a). As microstructural evidence
327 of garnet dissolution was completely absent from these small inclusions, we ascribed this
328 phenomenon to the fact that the excitation volume created by the beam also included a portion of
329 the host. Analyses from inclusions below 5 μm were then removed from the dataset
330 (contaminated analyses are given in table S1). Based on such considerations, the high mafic
331 component of the melt preserved in these felsic granulites should be considered a primary feature.
332 CMT nanogranitoids have a very high FeO+MgO content when compared with experimental
333 melts from metasedimentary protoliths, i.e. 2.58-5.64 wt.% in the CMT nanogranitoids (on

anhydrous basis) versus 0.9-3.9 wt.% of the experimental dataset compiled by Stevens et al. (2007). The database of nanogranitoids and melt inclusions (Bartoli et al., 2016) shows that most of the melt inclusions (for a total of ~600 analyses in 2016) have a FeO+MgO+TiO_2 content in the range 0.25-2.50 wt.%, with only ~10% of the whole database having contents 4 - 5 wt.%. As CMT nanogranitoids show an average FeO+MgO+TiO_2 =4.32 wt.% (Table 2), their mafic component is higher than almost 90% of the anatectic melt inclusions measured so far.

Experimental work on Fe and Mg contents in haplogranitic melts (Johannes and Holtz, 1996) and melting experiments on metasediments (Patiño-Douce and Johnston, 1991; Montel and Vielzeuf, 1997; Droop et al., 2003) show that a granitic melt produced during melting of metasediments can accommodate a progressively higher amount of Fe and Mg as the formation *T* of the melt increases. Such observations, so far rooted exclusively in experimental findings, are now supported by our natural data. This is clearly visible when they are plotted against data available in literature on granitic inclusions from metasediments melted at different *T* (Fig. 7; see also Table 2). Different case studies of nanogranitoids show a positive correlation between melting *T* (corresponding in turn to melt entrapment in the growing host) and FeO+MgO content. Indeed, the melt in the CMT nanogranitoids, which shows the highest FeO+MgO content among all the granitic inclusions, formed at $T \geq$ 1000°C, the highest formation *T* identified so far in nanogranitoids from metasediments. Conversely, the melt produced at lower *T*, 700-710°C, shows the lowest FeO+MgO content, in the range 1.34-1.83 wt.%.

Variable degrees of FeO+MgO enrichment are commonly observed in leucosomes from partially melted metasediments and in S-type granites (Stevens et al., 2007; Villaros et al., 2009), commonly associated to an increase in A/CNK and a decrease in silica content (Taylor and Stevens, 2012). This has been proposed to be the result of selective entrainment in the magma of

peritectic garnet, the most common repository of Fe, Mg and Al in metamorphosed crustal rocks, as the melt progressively coalesces at depth and migrates upwards (Stevens et al., 2007). This hypothesis assumes that most pristine anatectic melts from metasediments are leucogranitic and very low in mafic components, a concept so far supported by both experiments (Stevens et al., 2007) and melt inclusions (Bartoli et al., 2016). However, our study demonstrates that anatectic melts can instead show a rather high content of Fe and Mg when produced at T>1000°C and, thus, they should be considered to have a pristine, "starting" composition (Ferrero et al., 2012; Bartoli et al., 2016). This observation does not affect the validity of the peritectic phase entrainment hypothesis, which remains a sound explanation for FeO+MgO enrichment in S-type granites. It does however pose a significant caveat for researchers who want to correctly estimate the magnitude of peritectic phase entrainment experienced by the granitic body/leucosome under investigation, warning in particular against overestimating the magnitude of entrainment by assuming a too small FeO+MgO content in the original anatectic melt when the latter is produced at T in excess of 950-1000 °C.

Volatiles in high pressure melt

H_2O is necessary to stabilize any silicate melt under crustal conditions, and the quantification of H_2O, as well as of other species such as CO_2 and halogens, partitioned into deep partial melts is of utmost importance for quantifying volatile cycles at depth and how they affect deep melting processes (Bartoli et al., 2014). NanoSIMS analyses on re-homogenized nanogranitoids is a routine approach in nanogranitoid studies (e.g. Acosta-Vigil et al. 2016), and it has shown that nanogranitoids generally preserve their original composition in terms of H_2O (Bartoli et al., 2014) and CO_2 contents (Carvalho et al., 2019). In particular, the loss of H_2O (even as OH) from the

380 inclusion to the matrix surrounding the garnet would shift the liquidus of the trapped melt toward
381 higher T (Johannes and Holtz, 1996). Thus the nanogranitoids would re-homogenize only at *T*
382 significantly higher than those obtained via independent geothermobarometry on the host rocks,
383 which is not the case here: the inclusions re-homogenize indeed at ~1050°C, consistently with the
384 *T* range of Zr-in-Rt thermometers on the rutile needles present in the nanogranitoid-bearing
385 garnets (Axler and Ague, 2015). In this work, the average H_2O value (4.40 wt.%) is rather close
386 to that obtained via difference from 100 of the EMP totals after alkali loss correction (4.74 wt.%).
387 Both values are consistent with experimental estimates of H_2O content in haplogranitic melts at
388 the PT conditions of interest, as the experimental parameters of the two successful experiments
389 (point 3,4 and 5 in Fig. 2) are close to the 4 wt.% H_2O liquidus curve extrapolated at P >1.0 GPa
390 (Johannes and Holtz, 1996). Such values fit remarkably well also with the recent results of
391 Makhluf et al. (2017) on granite formation at 1.0 GPa.

392 The melt also contains significant amounts of CO_2, on average ~ 3000 ppm (0.3 wt.%). This
393 CO_2 may be internally produced as result of the devolatilization of hydrous silicates in the
394 presence of graphite (Connolly and Cesare, 1993; Cesare et al., 2005) visible in the CMT felsic
395 granulites as trapped minerals in inclusions and/or as mineral inclusions in garnet and the rock
396 matrix (Axler and Ague 2015). The CO_2 content of the CMT nanogranitoids is higher, on
397 average, than in the nanogranitoids measured in the graphite-bearing metasediments of the Ivrea-
398 Verbano Zone (IVZ; Carvalho et al., 2019), the only other case study so far where CO_2 was
399 measured *in situ* in re-homogenized nanogranitoids. It is likely that the different depth at which
400 melting occurred played a major role in shaping the CO_2 content of the melt. Experimental
401 studies have shown that CO_2 solubility in melt increases dramatically with increasing P (~500
402 ppm each 0.1 GPa in experimental studies; Ni and Keppler, 2013), and in fact our results show

403 that CMT nanogranitoids likely formed at significantly greater depth than IVZ nanogranitoids,
404 1.7-2.0 GPa (this study) vs. 0.8 GPa (Carvalho et al., 2019).

405 Probably the most striking feature of the CMT melt is the presence of a significant amount of
406 halogens. Chlorine (0.32 wt.% average) and F (3161 ppm, or ~0.32 wt.%) account together for
407 0.64 wt.% on average of the total melt composition. This is also consistent with the fact that
408 phlogopite crystallized inside the CMT nanogranitoids has been found, in one case, to contain an
409 unusually high amount of F (>1 wt.%; Axler and Ague, 2015). Halogens are characteristic of
410 brines, i.e. saline and Cl-rich fluid with low H_2O activity, proposed by some authors to play an
411 important role in the melting processes occurring in a thickened crust at either lower crustal or
412 upper mantle conditions (Aranovich et al., 2014). The Cl content of partial melts can be used as
413 proxy for the presence of brines during melt production at depth (Acosta-Vigil et al., 2016). CMT
414 nanogranitoids contain 0.10-0.97 wt.% of Cl, an amount comparable to those reported in
415 experimental melts coexisting with brines, i.e., ranging between ~0.2 and 1.6 wt.% (Webster and
416 Mandeville, 2007; Aranovich et al., 2013; Safonov et al., 2014).

417 Based on the extrapolation of existent experimental results on haplogranite melting in presence
418 of H_2O-NaCl-KCl (750-950°C / 0.6-1.4 GPa; Aranovich et al., 2013), the brine originally present
419 at >1000°C and 2.0 GPa in the CMT granulites likely had X_{H2O} ~0.3 (see Fig. 3 and 8 in
420 Aranovich et al., 2013). More precise estimates are hampered by the lack of leftover fluid, i.e.
421 primary fluid inclusions or detectable fluid in nanogranitoids, as well as of more precise
422 experimental constraints e.g. on CO_2 and F- bearing systems at conditions closer to those of
423 interest. Experiments show furthermore that brines in a haplogranitic system may cause a
424 significant shift of the minimum melting *T* toward higher values due to the lowering of the H_2O
425 activity (Aranovich et al., 2013; Aranovich, 2017). This would help to create the conditions for

This is the peer-reviewed, final accepted version for American Mineralogist, published by the Mineralogical Society of America.
The published version is subject to change. Cite as Authors (Year) Title. American Mineralogist, in press.
DOI: https://doi.org/10.2138/am-2021-7690. http://www.minsocam.org/

426 melting to occur at extreme *T* (>1000°C) as proposed for the CMT felsic granulites, a notion
427 independently supported by both previous PT estimates (Ague et al., 2013; Axler and Ague,
428 2015) as well as by the complete re-homogenization of the nanogranitoids at 1050°C. Another
429 possibility is that the enrichment in halogens predated the metamorphic peak, i.e. the brines were
430 not present during melting but had infiltrated the felsic granulites during their prograde
431 metamorphic evolution. In this scenario, Cl and F may be incorporated in the biotite, and this
432 process extends biotite stability field toward UHT conditions (Kelsey and Hand, 2015), thus
433 allowing biotite to destabilize at significantly higher *T* than commonly expected.
434
435 **IMPLICATIONS and CONCLUSIONS**
436 The deep nature of granulite metamorphism and the high thermal flux required to achieve
437 melting favor post-melting re-equilibration and re-crystallization of granulites/migmatites, often
438 obliterating the most direct evidence of the presence of melt, such as leucosomes and melt
439 pseudomorphs (White et al., 2011). For this reason, the preserved melt inclusions sheltered in
440 peak peritectic garnet of the CMT felsic granulites are a crucial finding. They indeed provide new
441 data necessary to create a more comprehensive portrait of the multiple aspects of melting, melt
442 preservation, and crustal evolution during metamorphism in the deep roots of orogens. In
443 particular:
444 • HP melts from metasediments are still underrepresented in the nanogranitoid database, as
445 the bulk of the reported case studies are from rocks melted at P ≤1.5 GPa (see lists in Cesare et
446 al., 2015; Bartoli et al., 2016; Acosta-Vigil et al., 2016; Ferrero et al. 2018b), with only one case
447 at significantly greater depth >4.5 GPa (Stepanov et al 2016). Our data are thus a step toward
448 filling the gap in knowledge on natural partial melts forming at intermediate P (~2.0 GPa), along

449 with the recent work on metasomatic nanogranitoids, originally from melting of crustal
450 sedimentary rocks and now hosted in the Granulitgebirge pyroxenites (Borghini et al., 2018;
451 2020). A further important feature of the CMT nanogranitoids is the fact that they are richer in
452 mafic components (FeO and MgO) than the majority of nanogranitoid case studies, regardless of
453 the protolith. Their pristine nature thus provides a direct confirmation that the granitic melt from
454 anatexis can accommodate an increasing amount of Fe and Mg with increasing T, an observation
455 rooted until now exclusively in experimental studies. This finding is thus a caveat against
456 assuming that natural pristine anatectic melts are always leucogranitic.

457 • Our independent experimental results provide the first evidence of HP conditions during
458 the metamorphic peak / melting of the felsic granulites in the Central Maine Terrane, pointing
459 toward melting conditions of ~1050°C and 1.7-2.0 GP. HP metamorphism, rather than purely
460 UHT (Ague et al., 2013), is also supported by the widespread presence of pseudomorphs of
461 sillimanite after kyanite in the matrix (Axler and Ague, 2015). Our findings warrant a reappraisal
462 of the metamorphic peak conditions in the area and finds direct support in other recent studies in
463 nearby localities: HP conditions (1.8 GPa) reported in silica-undersaturated gneisses (Keller and
464 Ague, 2018), whereas other metapelites contain evidence of UHP metamorphism (>5 GPa; Keller
465 and Ague, 2020);

466 • H_2O, CO_2, Cl and F were measured directly in situ in the HP crustal melt still preserved in
467 its original source rock. H_2O was previously measured in nanogranitoids from rocks equilibrated
468 between ~0.4 GPa and 1.4 GPa (Bartoli et al., 2014; 2016; Acosta-Vigil et al., 2016; Carvalho et
469 al., 2019), whereas in situ CO_2 measurements are only available from the IVZ, equilibrated at 0.8
470 GPa (Carvalho et al. 2019). Our new measurements extend the existing dataset toward
471 significantly greater depth and provide the foundation of further studies to further clarify how the

472 interplay of protolith, fluid speciation, and PT conditions influence H_2O and carbon budgets
473 during crustal subduction and thickening. Moreover, to our knowledge, our study presents the
474 first data on F measured in situ in anatectic melt inclusions. Previous experimental studies
475 suggest that the presence of a significant amount of Cl, such as measured in the CMT inclusions,
476 may be indicative of the presence of saline fluids (brines) during melting. This is the first direct
477 natural evidence that brines infiltrating the lower crust as a metasomatic fluid may be an
478 influential factor for the establishment of conditions necessary to produce melt at such extreme *T*
479 (>1000°C), commonly inferred to be characterized by fluid-absent melting conditions.
480
481 Acknowledgements
482 The present research was funded by the German Federal Ministry for Education and Research
483 and the Deutsche Forschungsgemeinschaft (Project FE 1527/2-1 and FE 1527/2-2) to SF. JJA
484 gratefully acknowledges support from the National Science Foundation (EAR-1250269 and
485 EAR-1753553) and Yale University. The NanoSIMS facility at the Muséum National d'Histoire
486 Naturelle in Paris was established by funds from the CNRS, Région Ile de France, Ministère
487 délégué à l'Enseignement supérieur et à la Recherche, and the Muséum National d'Histoire
488 Naturelle. Our deepest thanks go to C. Günter, F. Kaufmann and L. Hecht for help during
489 analyses, and to C. Fischer for sample preparation. The authors are grateful to H. Lamadrid and
490 an anonymous reviewer for their insightful comments which improved the quality of the paper,
491 and to M. Steele-McInnis for his careful editorial handling.
492
493 *References*

494 Acosta-Vigil, A., Barich, A., Bartoli, O., Garrido, C.J., Cesare, B., Remusat, L., Poli, S.,
495 andRaepsaet, C. (2016). The composition of nanogranitoids in migmatites overlying the Ronda

peridotites (Betic Cordillera, S Spain): the anatectic history of a polymetamorphic basement. Contributions to Mineralogy and Petrology, 171, 24.

Acosta-Vigil, A., Cesare, B., London, D., Morgan, G. B., VI (2007). Microstructures and composition of melt inclusions in a crustal anatectic environment, represented by metapelitic enclaves within El Hoyazo dacites, SE Spain. Chemical Geology 235, 450-465.

Ague, J.J., Eckert, J.O. Jr., Chu, X., Baxter, E.F., and Chamberlain, C.P. (2013) Discovery of ultrahigh-temperature metamorphism in the Acadian orogen, Connecticut, USA. Geology, 41, 271–274.

Aranovich, L.Y., Makhluf, A.R., Manning, C.E., and Newton, R.C. (2014) Dehydration melting and the relationship between granites and granulites. Precambrian Research, 253, 26–37.

Aranovich, L.Y., Newton, R.C., and Manning, C.E. (2013) Brine-assisted anatexis: experimental melting in the system haplogranite–H_2O–NaCl–KCl at deep-crustal conditions. Earth and Planetary Science Letters 374, 111-120.

Auzanneau, E., Vielzeuf, D., and Schmidt, M.W. (2006) Experimental evidence of decompression melting during exhumation of subducted continental crust. Contributions to Mineralogy and Petrology, 152, 125–148.

Axler, J.A., and Ague, J.J. (2015) Oriented multiphase needles in garnet from ultrahigh-temperature granulites. American Mineralogist, 100, 2254–2271.

Bartoli, O., Acosta-Vigil, A., Ferrero, S., and Cesare, B. (2016) Granitoid magmas preserved as melt inclusions in high-grade metamorphic rocks. American Mineralogist, 101, 1543–1559.

Bartoli, O., Acosta-Vigil, A., Cesare, B., Remusat, L., Gonzalez-Cano, A., Wälle, M., Tačjmanová, L., Langone, A. (2019) Geochemistry of Eocene-early Oligocene low-temperature crustal melts from Greater Himalayan Sequence (Nepal): a nanogranitoid perspective. Contributions to Mineralogy and Petrology, 174, 82.

Bartoli, O., Cesare, B., Poli, S., Acosta-Vigil, A., Esposito, R., Turina, A., Bodnar, R.J., Angel, R.J., and Hunter, J. (2013a) Nanogranite inclusions in migmatitic garnet: Behavior during piston cylinder re-melting experiments. Geofluids, 13, 405–420.

Bartoli, O., Cesare, B., Poli, S., Bodnar, R.J., Acosta-Vigil, A., Frezzotti, M.L., and Meli, S. (2013b) Recovering the composition of melt and the fluid regime at the onset of crustal anatexis and S-type granite formation. Geology, 41, 115–118.

Bartoli, O., Cesare, B., Remusat, L., Acosta-Vigil, A. and Poli, S. (2014) The H_2O content of granite embryos. Earth and Planetary Science Letters 395, 281-290.Borghini, A., Ferrero, S., Wunder, B., Laurent, O., O'Brien, P. J., and Ziemann, M. A. (2018) Granitoid melt inclusions in orogenic peridotite and the origin of garnet clinopyroxenite. Geology, 46(11), 1007–1010.

Borghini, A., Ferrero, S., O'Brien, P. J., Laurent, O., Günter, C., and Ziemann, M. A. (2020) Cryptic metasomatic agent measured in situ in Variscan mantle rocks: Melt inclusions in garnet of eclogite, Granulitgebirge, Germany. Journal of Metamorphic Geology, 38, 207–234.

Brown, M., 2006. Duality of thermal regimes is the distinctive characteristic of plate tectonics since the Neoarchean. Geology, 34, 961-964.

Bureau, H., Trocellier, P., Shaw, C., Khodja, H., Bolfan-Casanova, N., Demouchy, S., 2003. Determination of the concentration of water dissolved in glasses and minerals using nuclear microprobe. Nucl. Instrum. Methods Phys. Res., Sect. B 210, 449–454.

Carvalho, B. B., Bartoli, O., Ferri, F., Cesare, B., Ferrero, S., Remusat, L., Capizzi, L.S., Poli, S. (2019). Anatexis and fluid regime of the deep continental crust: New clues from melt and fluid inclusions in metapelitic migmatites from ivrea zone (NW italy). Journal of Metamorphic Geology, 37, 951-975. 63

Connolly, J. A. D. And Cesare, B. (1993) C-O-H-S fluid composition and oxygen fugacity in graphitic metapelites. Journal of Metamorphic Geology, 11, 368-378.

Cesare, B., Acosta-Vigil, A., Bartoli, O., and Ferrero, S. (2015) What can we learn from melt inclusions in migmatites and granulites? Lithos, 239, 186–216.

Cesare, B., Meli, S., Nodari, L., and Russo, U., (2005) Fe3+ reduction during biotite melting in graphitic metapelites: another origin of CO2 in granulites. Contributions to Mineralogy and Petrology, 149, 129–140.

Cesare, B., Ferrero, S., Salvioli-Mariani, E., Pedron, D., and Cavallo, A. (2009) Nanogranite and glassy inclusions: the anatectic melt in migmatites and granulites. Geology, 37, 627–630.

Créon, L., Levresse, G., Remusat, L., Bureau, H. and Carrasco-Núñez, G. (2018) New method for initial composition determination of crystallized silicate melt inclusions. Chemical Geology 483, 162-173.

Darling, R. S., Chou, I.-M., and Bodnar, R. J. (1997) An occurrence of metastable cristobalite in high-pressure garnet granulite. Science, 276, 91–93.

Droop, G.T.R., Clemens, J.D., and Dalrymple, J. (2003) Processes and conditions during contact anatexis, melts escape and restite formation: The Huntly Gabbro complex, NE Scotland. Journal of Petrology, 44, 995–1029.

Ferrero, S., and Angel, R. J. (2018) Micropetrology: are inclusions in minerals grains of truth? Journal of Petrology, 59, 1671–1700.

Ferrero, S., Bodnar, R.J., Cesare, B., and Viti, C. (2011) Reequilibration of primary fluid inclusions in peritectic garnet from metapelitic enclaves, El Hoyazo, Spain. Lithos, 124, 117–131.

Ferrero, S., Bartoli, O., Cesare, B., Salvioli-Mariani, E., Acosta-Vigil, A., Cavallo, A., Groppo, C., and Battiston, S. (2012) Microstructures of melt inclusions in anatectic metasedimentary rocks. Journal of Metamorphic Geology, 30, 303–322.

Ferrero, S., Wunder, B., Ziemann, Wälle, M., and O'Brien, P.J. (2016a) Carbonatitic and granitic melts produced under conditions of primary immiscibility during anatexis in the lower crust. Earth Planetary Science Letters, 454, 121–131.

Ferrero, S., Ziemann, M.A., Angel, R.J., O'Brien, P.J. and Wunder, P.J. (2016b) Kumdykolite, kokchetavite, and cristobalite crystallized in nanogranites from felsic granulites, Orlica Snieznik Dome (Bohemian Massif): not evidence for ultrahigh pressure conditions. Contributions to Mineralogy and Petrology, 171, 3.

Ferrero, S., Godard, G., Palmeri, R., Wunder, B., and Cesare B. (2018a) Partial melting of ultramafic granulites from Dronning Maud Land, Antarctica: Constraints from melt inclusions and thermodynamic modelling. American Mineralogist, 103, 610-622.

Ferrero, S., O'Brien, P. J., Borghini, A., Wunder, B., Wälle, M., Günter, C., and Ziemann, M. A. (2018b) A treasure chest full of nanogranitoids: an archive to investigate crustal melting in the Bohemian Massif, in Ferrero, S., Lanari, P., Goncalves, P., and Grosch, E. G., eds., Metamorphic Geology: Microscale to Mountain Belts: Geological Society, London, Special Publications 478, 13-38.

Ferrero, S., Wunder, B., Walczak, K., Ziemann, M.A., O'Brien, P.J. (2015) Preserved near ultrahigh-pressure melt from continental crust subducted to mantle depths. Geology, 43, 447-450.

Ferri, F., Cesare, B., Bartoli, O., Ferrero, S., Palmeri, R., Remusat, L., Poli, S. (2020) Melt inclusions at MT. Edixon (Antarctica): Chemistry, petrology and implications for the evolution of the Lanterman range. Lithos, 374–375, 105685.

Gianola, O., Bartoli, O., Ferri, F., Galli, A., Ferrero, S., Capizzi, L.S., Liebske, C., Remusat,. L., Poli, S., Cesare, B. (2020) Anatectic melt inclusions in ultra-high temperature granulites. Journal of Metamorphic Geology, accepted.

Hauri, E., Wang, J., Dixon, J.E., King, P.L., Mandeville, C. and Newman, S. (2002) SIMS analysis of volatiles in silicate glasses: 1. Calibration, matrix effects and comparisons with FTIR. Chemical Geology 183, 99-114.

Hwang, S-L., Shen, P., Chu, H-T., Yui, T-F, Liou, J-G., Sobolev, N.V., Zhang, R.Y., Shatsky, V.S., and Zayachkovsky, A.A. (2004) Kokchetavite: a new polymorph of KAlSi3O8 from the Kokchetav UHP terrain. Contributions to Mineralogy and Petrology, 148: 380–389.

Keller, D. S., and Ague, J. J. (2018) High-pressure granulite facies metamorphism (~1.8 GPa) revealed in silica-undersaturated garnet-spinel-corundum gneiss, Central Maine Terrane, Connecticut, U.S.A. American Mineralogist, 103, 1851–1868.

Keller, D. S., and Ague, J. J. (2020) Quartz, mica, and amphibole exsolution from majoritic garnet reveals ultra-deep sediment subduction, Appalachian orogeny. Science Advances, 6, 11.

Kelsey,D.E. (2008) On ultrahigh-temperature crustal metamorphism. Gondwana Research, 13: 1–29.

Kelsey, D.E., and Hand, M. (2015) On ultrahigh temperature crustal metamorphism: Phase equilibria, trace element thermometry, bulk composition, heat sources, timescales and tectonic settings. Geoscience Frontiers, 6, 311-356.

Johannes, W., and Holtz, F. (1996) Petrogenesis and experimental petrology of granitic rocks, 335 p. Berlin, Springer.

Le-Breton, N., and Thompson, A.B. (1988) Fluid-absent (dehydration) melting of biotite in metapelites in the early stages of crustal anatexis. Contributions to Mineralogy and Petrology, 99, 226–237.

Makhluf, A. R., R. C. Newton, and C. E. Manning (2017) Experimental determination of liquidus H2O contents of haplogranite at deep-crustal conditions. Contributions to Mineralogy and Petrology, 172, 77.

Mirwald, P.W., Massonne, H.-J. (1980) Quartz-coesite transition and the comparative friction measurements in piston-cylinder apparatus using talc-alsimag glass (TAG) and NaCl high pressure cells: a discussion. Neues Jahrbuch für Mineralogie, 469-477.

Morgan G.B.VI, and London, D. (2005) Effect of current density on the electron microprobe analysis of alkali aluminosilicate glasses. American Mineralogist, 90, 1131–1138.

Montel, J.-M., and Vielzeuf, D. (1997). Partial melting of metagreywackes, Part II. Compositions of minerals and melts. Contributions to Mineralogy and Petrology, 128, 176–196.

Ni, H., and Keppler, H. (2013). Carbon in silicate melts. Reviews in Mineralogy & Geochemistry, 75, 251-287.

O'Brien, P.J., and Ziemann, M.A. (2008) Preservation of coesite in exhumed eclogite: insights from Raman mapping. European Journal of Mineralogy, 20, 827-834.

Patiño Douce, A.E., and Johnston, A.D. (1991) Phase equilibria and melt productivity in the pelitic system: implications for the origin of peraluminous granitoids and aluminous granulites. Contributions to Mineralogy and Petrology 107, 202–218.

Pownall, J.M., Armstrong, R.A., Williams, I.S., Thirlwall, M.F., Manning, C.J. & Hall, R. (2018). Miocene UHT granulites from Seram, eastern Indonesia: a geochronological–REE study of zircon, monazite and garnet, in Ferrero, S., Lanari, P., Goncalves, P., and Grosch, E. G., eds., Metamorphic Geology: Microscale to Mountain Belts: Geological Society, London, Special Publications 478, 167-196.

633 Safonov, O.G., Kosova, S.A., and van Reenen, D.D. (2014) Interaction of biotite-amphibole
634 gneiss with H_2O–CO_2–(K, Na)Cl fluids at 550 MPa and 750 and 800 °C: experimental study and
635 applications to dehydration and partial melting in the middle crust. Journal of Petrology, 55,
636 2419–2456.
637 Stepanov, A.S., Hermann, J., Rubatto, D., Korsakov, A.V., Danyushevsky, L.V. (2016) Melting
638 History of an Ultrahigh-pressure Paragneiss Revealed by Multiphase Solid Inclusions in Garnet,
639 Kokchetav Massif, Kazakhstan. Journal of Petrology, 57, 1531-1554.
640 Stevens, G., Villaros, A., and Moyen, J.-F. (2007) Selective peritectic garnet entrainment as the
641 origin of geochemical diversity in S-type granites. Geology 35, 9–12.
642 Taylor, J., and Stevens, G. (2010). Selective entrainment of peritectic garnet into S-type
643 granitic magmas: evidence from Archaean mid-crustal anatectites. Lithos, 120, 277–292.
644 Tomkins, H.S., Powell, R., Ellis, D.J. (2007) The pressure dependence of the zirconium-in-
645 rutile thermometer. Journal of Metamorphic Geology, 25, 703–713.
646 Thomen, A., Robert, F. and Remusat, L. (2014) Determination of the nitrogen abundance in
647 organic materials by NanoSIMS quantitative imaging. Journal of Analytical Atomic
648 Spectrometry 29, 512-519.
649 Villaros, A., Stevens, G., Moyen, J.F., and Buick, I.S. (2009). The trace element compositions
650 of S-type granites: evidence for disequilibrium melting and accessory phase entrainment in the
651 source. Contributions to Mineralogy and Petrology, 158, 543–561.
652 Webster, J.D., and Mandeville, C.W. (2007) Fluid immiscibility in volcanic environments. In:
653 Liebscher A, Heinrich CA (eds) Fluid-fluid interactions. Reviews in Mineralogy and
654 Geochemistry, 65, 313–362.
655 White, R.W., Stevens, G., and Johnson, T.E. (2011) Is the crucible reproducible? Reconciling
656 melting experiments with thermodynamic calculations. Elements, 7, 241–246.
657 Whitney, D.L., and Evans, B.W. (2010) Abbreviations for names of rock-forming minerals.
658 American Mineralogist, 95, 185–187.
659

660 **CAPTIONS**

661 FIGURE 1. Microstructural features of inclusions and host rocks. (**a**) Scan of a representative
662 thick section with garnets in a more felsic matrix; the garnet in the upper left corner has a circle
663 made with a black marker. *White arrows:* MI-bearing garnets. Sample JAQ-124A. (**b**) Cluster of
664 polycrystalline inclusions occurring in the center of the garnet, mineral abbreviations from
665 Whitney and Evans (2010). *White arrows:* needle shaped nanogranitoids. Gray arrows: isometric
666 nanogranitoids, generally smaller than the first inclusion type. *Red arrows:* thin rutile needles. (**c**)
667 Close up of isometric nanogranitoids (**left**) with multiple birefringent phases visible under
668 crossed polars (**right**). (**d**) Close up of a needle shaped nanogranitoid (**left**), occasionally with the
669 rough outline already described by Axler and Ague (2015), and showing once again several
670 birefringent phases under crossed polars (**right**).

671

672 FIGURE 2. Results of MicroRaman investigation of a representative inclusion below the
673 surface (**a**). (**b**) Raman spectrum of cristobalite from the CMT nanogranitoids. (**c**) The map
674 shows the distribution of Raman peak 415 cm^{-1} of cristobalite (blue), 196 cm^{-1} of phlogopite
675 (green) and 963 cm^{-1} of apatite (red). In (**d**) also the distribution of peak 707 of white mica (red)
676 and the 675 cm^{-1} peak of ilmenite (green) are visible. In (e) the distribution of peak 430 cm^{-1} is
677 visible in green, whereas in (f) a representative spectrum of phase 430 is reported.

678

679 FIGURE 3: Experimental conditions (numbers in circles) versus previous estimates of
680 metamorphic peak equilibration for the host gneisses of the investigated nanogranitoids. Solid
681 lines: liquidus curves for different amount of H_2O according to Johannes and Holtz (1996).
682 AA15: Temperature and minimum P conditions proposed by Axler and Ague (2015) for the felsic

683 granulites investigated in the present study. KA18: HP conditions estimated on garnet-spinel-
684 corundum gneisses of the Central Maine Terrane by Keller and Ague (2018). Experiments 4 and
685 5 were conducted at the same conditions with different durations (see table 1).
686
687 FIGURE 4. BSE images of CMT nanogranitoids after piston cylinder experiments under
688 different confining *P*. *White arrows:* decrepitation cracks. *Red arrows*: new Mg-richer garnet.
689 See text for details on the single images.
690
691 FIGURE 5: composition of re-homogenized nanogranitoids. (**a**) Ab-Or-Qz and (**b**) Ab-Or-An
692 normative diagrams. (**c**) Alumina Saturation Index (ASI)= molar Al/(Ca+Na+K)) versus
693 Alkalinity Index (AI)= molar Al-(Na+K). (**d**) Silica content versus Modified Alkali-Lime Index
694 (MALI)= $Na_2O+K_2O–CaO$. CMT= central Maine Terrane; KKB= UHT nanogranites of the
695 Kerala Khondalite Belt (Ferrero et al., 2012). P91= experimental melts from Patiño-Douce and
696 Johnston (1991). For EMP compositions and *P-T* conditions of formation of the KKB and P91
697 melts see Table 2.
698
699 FIGURE 6: Raman spectrum of nanogranitoid re-homogenized to glass.
700
701 FIGURE 7: NanoSIMS measurements on re-homogenized nanogranitoids. (**a**) Measurements of
702 H_2O, CO_2 and F presented according to the garnet chip in which they were measured. Variation
703 diagrams of (**b**) CO_2 and (**c**) F with respect to H_2O for each single NanoSIMS analysis, including
704 one inclusion with clear fluid loss (indicated in figure).

FIGURE 8. High FeO+MgO content in re-homogenized CMT nanogranitoids. (**a**) Comparison between inclusion with diameter ≥5 μm (orange circles) and <5 μm (yellow circles; visible in table S1). (**b**) FeO+MgO versus T diagram, comparing nanogranitoids compositions from this study with previous case studies of inclusions in partially melted rocks with metasedimentary protolith (including standard deviations; data from Table 2). For abbreviations see caption Table 2.

Table 1: Conditions, relevant info and results of piston cylinder experiments.

Table 2: Geochemistry and PT conditions of formation of re-homogenized melt inclusions (n=19) from the Central Maine Terrane, experimental melts from metasediments (P91= Patiño-Douce and Johnston, 1991) and averages of melt inclusion analyses from different case studies of metasediments melted under different conditions. KKB (Kerala Khondalite Belt, Southern India) and BAR (Barun gneiss, Himalaya) are from Ferrero et al., (2012). F16 = Oberpfalz migmatites from Ferrero et al. (2016). AAV16= Jubrique migmatites, Betic Cordillera (S Spain) from Acosta-Vigil et al., (2016). AAV07= Grt+Bt granulitic enclaves of El Hoyazo, Neogene Volcanic Province (S Spain) from Acosta-Vigil et al., (2007). F11= Spl-Crd granulitic enclaves of El Hoyazo from Ferrero et al. (2011). B13= Sierra Alpujata metatexites, Betic Cordillera (S Spain) from Bartoli et al., (2013).

Table 3. H_2O, CO_2 and F contents in re-homogenized inclusions measured by NanoSIMS.

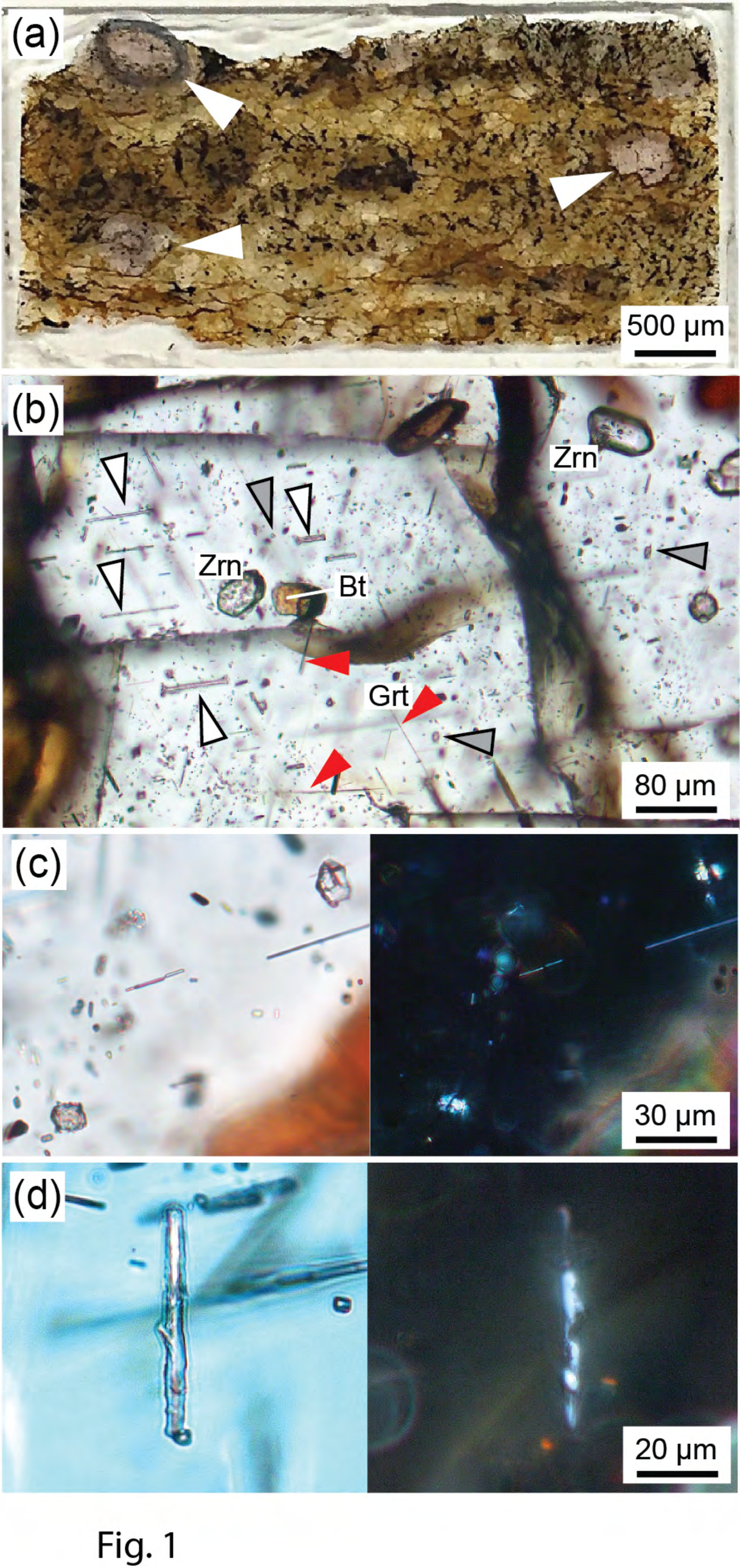

Fig. 1

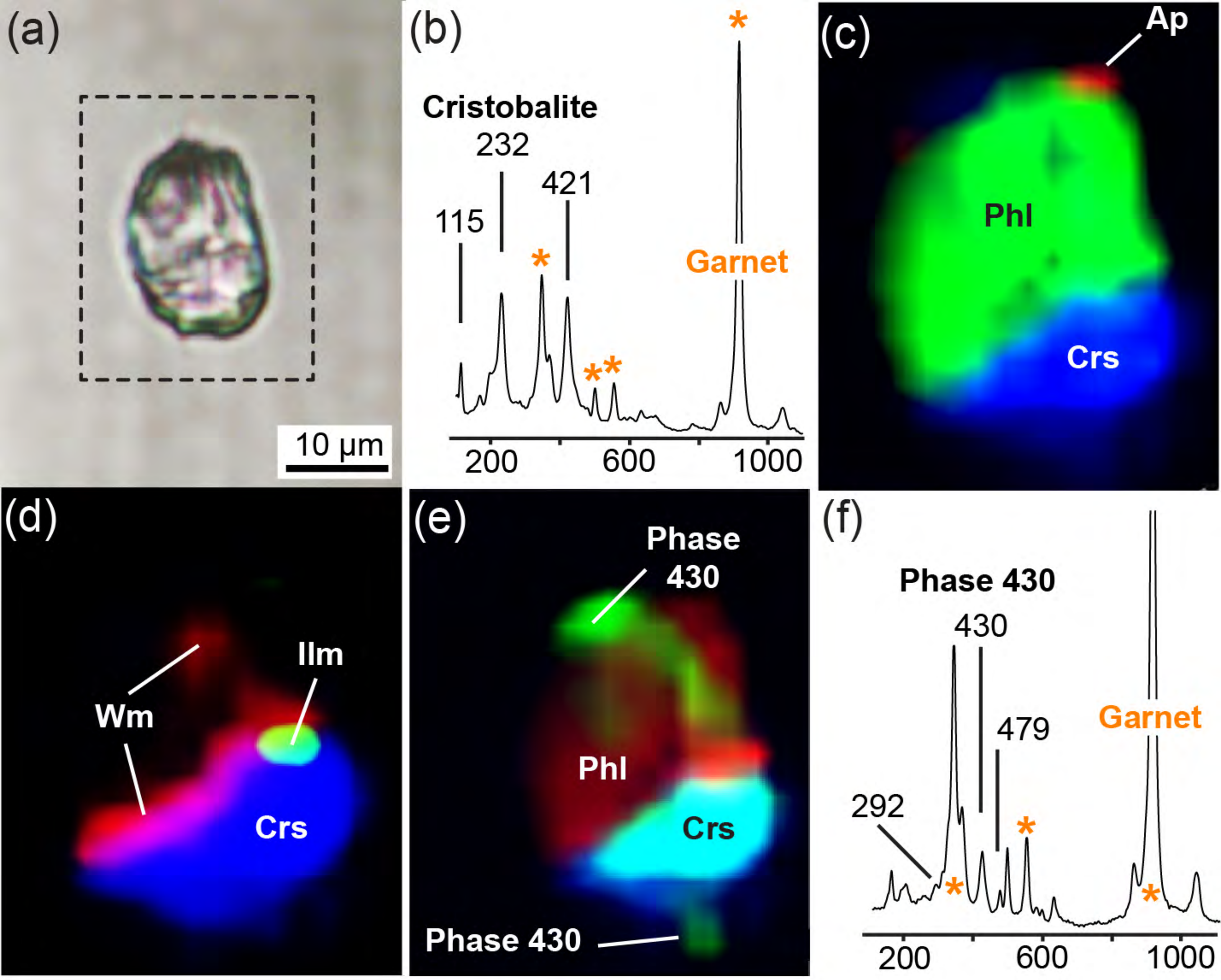
(a)
10 µm
(b)
Cristobalite
232
421
115
*
**
*
Garnet
200
600
1000
(c)
Ap
Phl
Crs
(d)
Wm
Ilm
Crs
(e)
Phase
430
Phl
Crs
Phase 430
(f)
Phase 430
430
479
292
*
*
*
Garnet
200
600
1000

Fig. 2

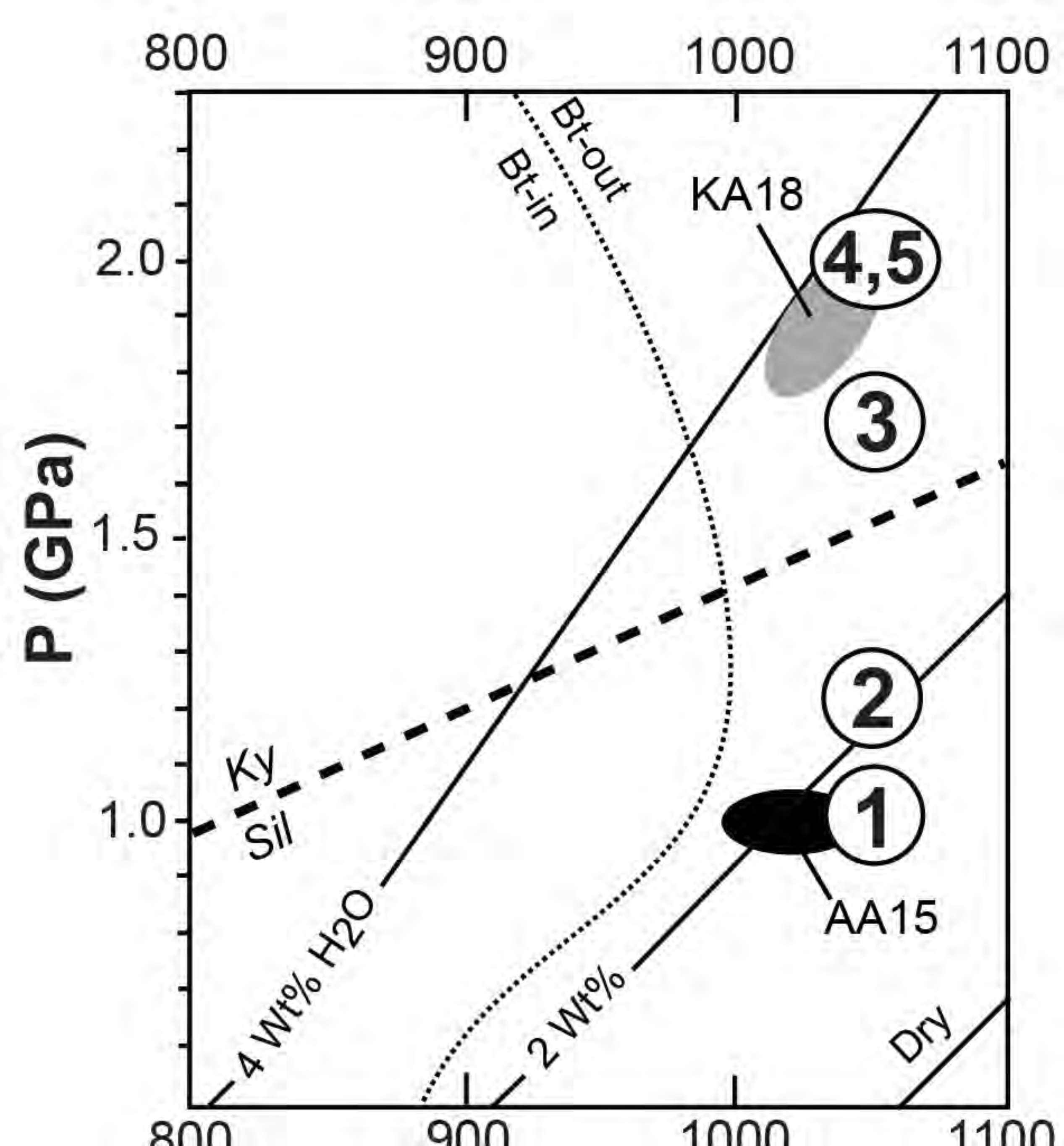
800
900
1000
1100
2.0
1.5
1.0
P (GPa)
Bt-out
Bt-in
KA18
4,5
3
2
1
AA15
Ky
Sil
4 Wt% H2O
2 Wt%
Dry
800
900
1000
1100
T (°C)

Fig. 3

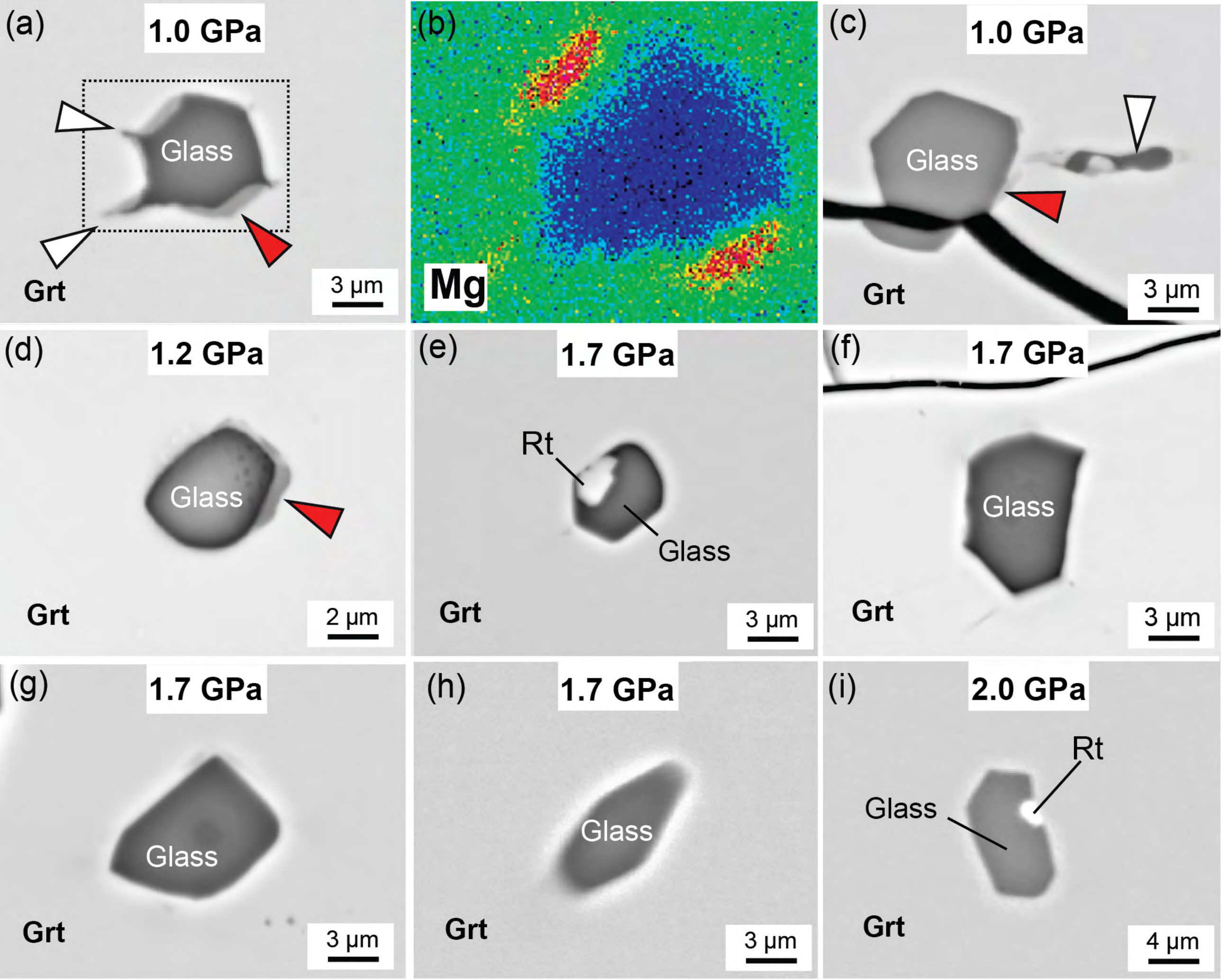
(a)
1.0 GPa
Glass
Grt
3 μm
(b)
Mg
(c)
1.0 GPa
Glass
Grt
3 μm
(d)
1.2 GPa
Glass
Grt
2 μm
(e)
1.7 GPa
Rt
Glass
Grt
3 μm
(f)
1.7 GPa
Glass
Grt
3 μm
(g)
1.7 GPa
Glass
Grt
3 μm
(h)
1.7 GPa
Glass
Grt
3 μm
(i)
2.0 GPa
Rt
Glass
Grt
4 μm

Fig. 4

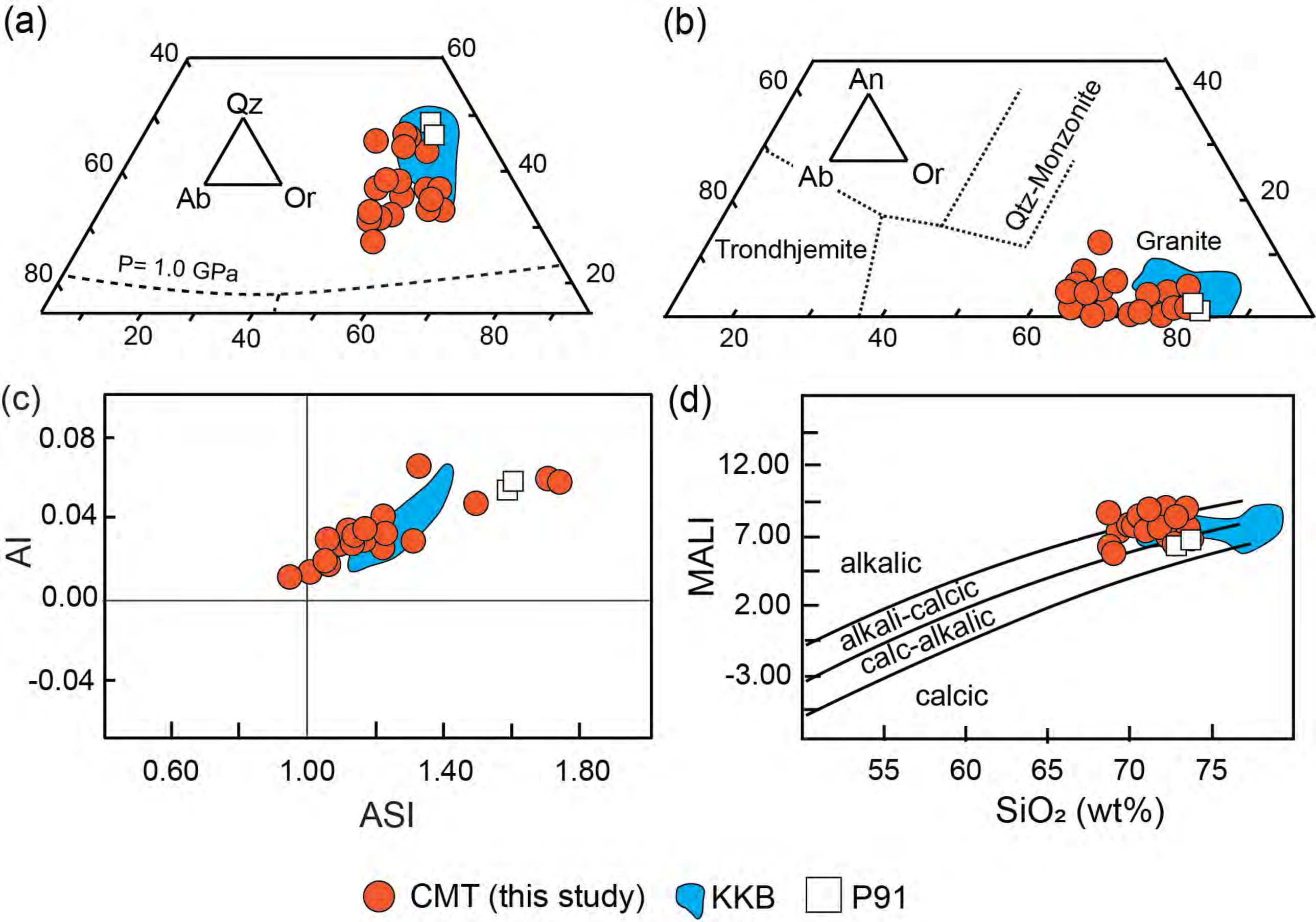
(a)
Qz
Ab
Or
P= 1.0 GPa
40
60
60
40
80
20
20
40
60
80
(b)
An
Ab
Or
Qtz-Monzonite
Trondhjemite
Granite
60
40
80
20
20
40
60
80
(c)
0.08
0.04
0.00
-0.04
ASI
0.60
1.00
1.40
1.80
(d)
12.00
7.00
2.00
-3.00
MALI
alkalic
alkali-calcic
calc-alkalic
calcic
55
60
65
70
75
SiO₂ (wt%)
CMT (this study)
KKB
P91

Fig. 5

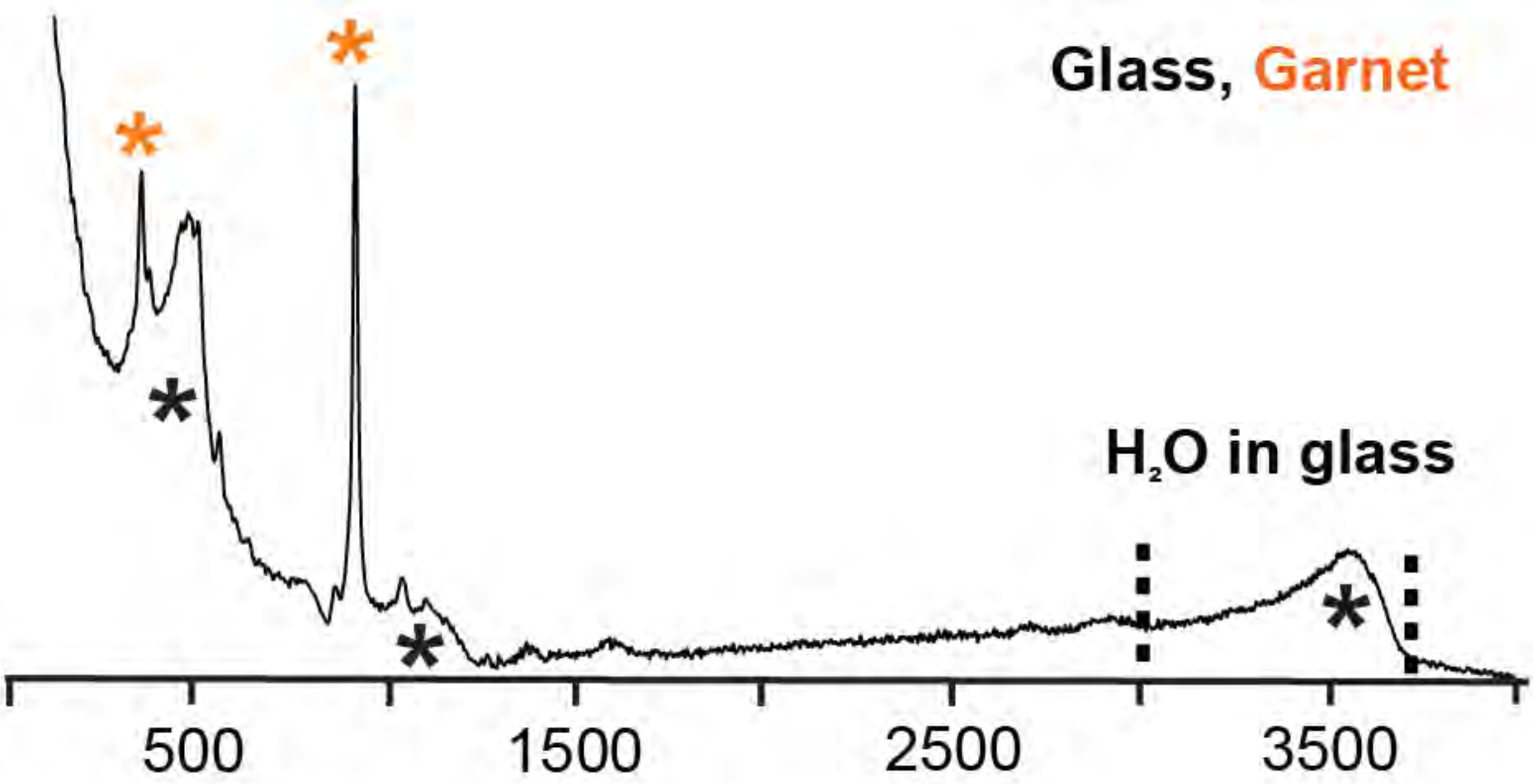
Glass, Garnet
H2O in glass
500
1500
2500
3500

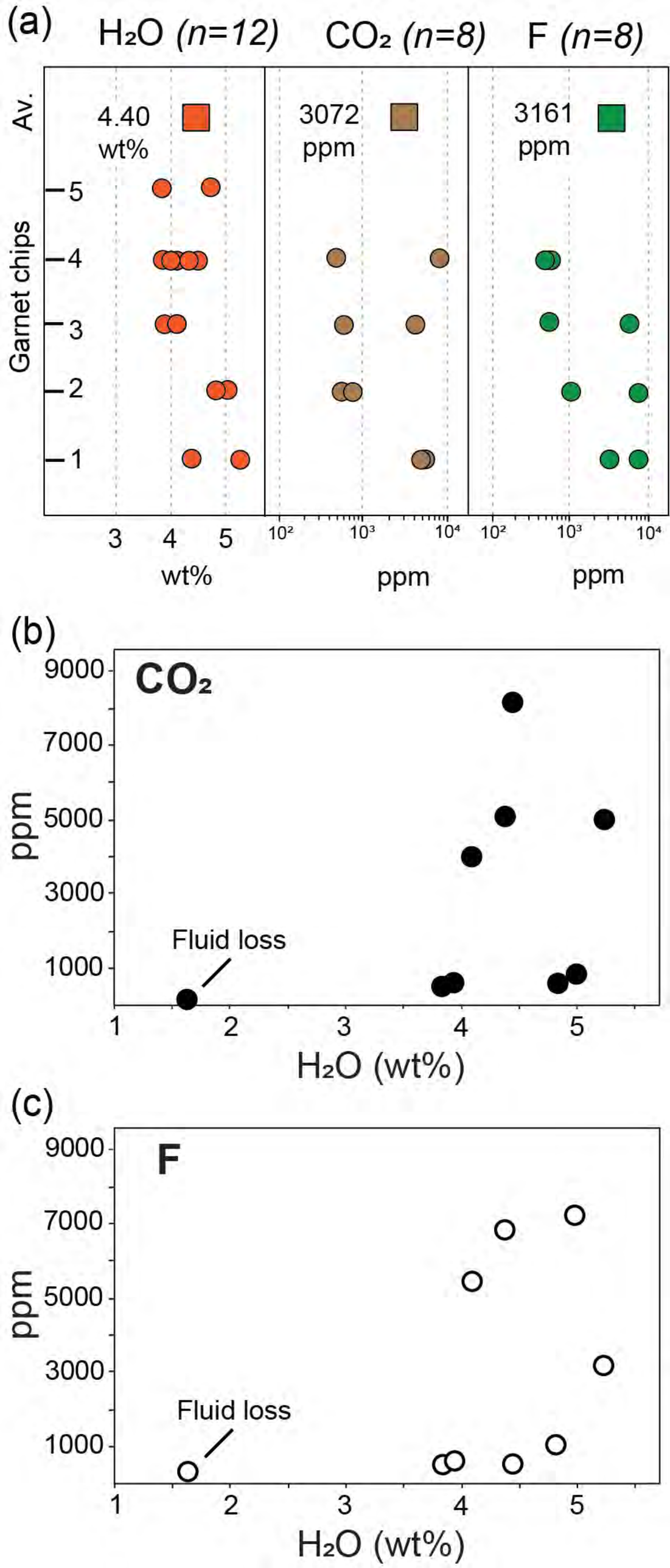
(a)
H₂O (n=12)
CO₂ (n=8)
F (n=8)
Av.
4.40 wt%
3072 ppm
3161 ppm
Garnet chips
5
4
3
2
1
3
4
5
10²
10³
10⁴
wt%
ppm
ppm
(b)
CO₂
9000
7000
5000
3000
1000
ppm
Fluid loss
1
2
3
4
5
H₂O (wt%)
(c)
F
9000
7000
5000
3000
1000
ppm
Fluid loss
1
2
3
4
5
H₂O (wt%)

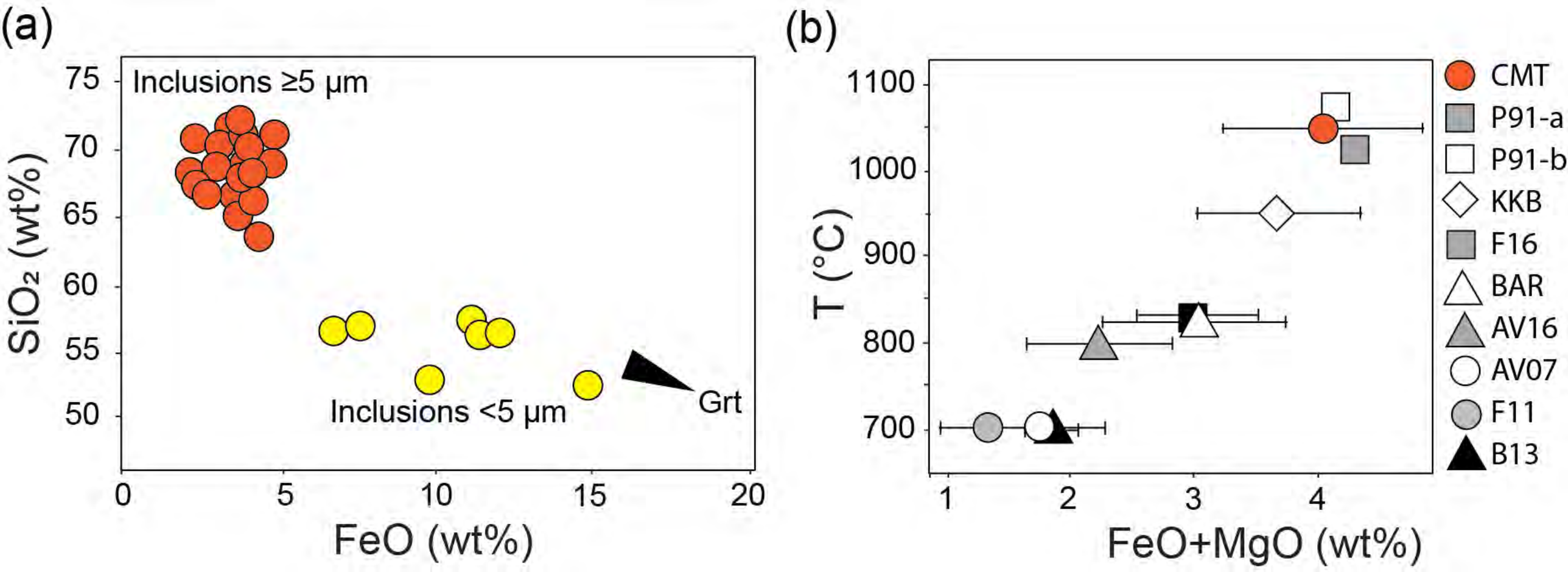
(a)
Inclusions ≥5 μm
Inclusions <5 μm
Grt
SiO2 (wt%)
FeO (wt%)
75
70
65
60
55
50
0
5
10
15
20
(b)
T (°C)
FeO+MgO (wt%)
1100
1000
900
800
700
1
2
3
4
CMT
P91-a
P91-b
KKB
F16
BAR
AV16
AV07
F11
B13

Experiment	Figures	T(°C)	P (GPa)	t (h)	Melting	Decrepitation
1	Fig. 4a,b,c	1050	1.0	≈15	X	X (extensive)
2	Fig. 4d	1050	1.2	24	X	-
3	Fig. 4e,f,g,h	1050	1.7	24	X	-
4	Fig. 4i	1050	2.0	24	X	-
5	-	1050	2.0	4	X	-

Melt-host interaction	Full Re-homogenization
X (new Grt+New Opx)	-
X (new Grt)	-
-	X
-	X
-	X

Central Maine Terrane

Name	21	43	av.44-4	18	20	21	22	23	24	7	8
Duration	*24h*	*24h*	*24h*	*24h*	*24h*	*24h*	*24h*	*24h*	*24h*	*24h*	*24h*
T (°C)	*1050*	*1050*	*1050*	*1050*	*1050*	*1050*	*1050*	*1050*	*1050*	*1050*	*1050*
P (Gpa)	*1.7*	*1.7*	*1.7*	*1.7*	*1.7*	*1.7*	*1.7*	*1.7*	*1.7*	*1.7*	*1.7*
Wt%											
SiO_2	64.96	68.89	63.61	67.10	69.15	68.22	67.64	66.00	68.32	66.80	67.30
TiO_2	0.64	0.36	0.03	0.05	0.91	0.24	0.14	0.14	0.10	0.05	0.16
Al_2O_3	12.61	12.50	14.74	12.39	12.96	12.89	13.80	12.42	13.71	12.84	14.03
FeO	3.71	4.76	4.43	3.27	3.22	3.53	3.25	4.10	3.08	2.89	2.38
MnO	0.11	0.11	0.04	0.02	0.09	0.14	0.02	0.08	0.01	0.00	0.00
MgO	0.61	0.58	0.63	1.11	0.38	0.41	0.70	1.01	0.63	0.57	0.30
CaO	1.17	0.98	1.68	0.01	0.36	0.14	0.12	0.36	0.03	0.94	0.55
Na_2O	1.32	1.28	1.58	1.71	1.28	1.50	1.66	1.17	1.14	1.89	1.68
K_2O	6.93	7.00	5.11	6.10	7.23	7.17	4.71	5.23	5.51	6.01	7.41
P_2O_5	0.59	0.75	0.28	0.05	0.18	0.15	0.16	0.12	0.07	0.23	0.19
Cl	0.07	0.21	0.08	0.86	0.82	0.68	0.95	0.93	0.97	0.01	0.04
Total	92.64	97.21	92.12	91.79	95.76	94.38	92.20	90.62	92.59	96.17	98.00
Q	26	30	27	29	31	29	36	34	37	32	30
C	2	3	4	3	3	3	6	4	6	2	2
Or	41	41	30	36	43	42	28	31	33	37	45
Ab	11	11	13	14	11	13	14	10	10	15	14
An	2	0	7	0	1	0	0	1	0	3	1
Hy	7	10	10	9	6	7	8	10	7	7	5
ASI	1.07	1.09	1.32	1.31	1.22	1.23	1.71	1.51	1.74	1.11	1.16
H_2O by diff	7.36	2.79	7.88	8.21	4.24	5.62	7.80	9.38	7.41	3.83	2.00
Mg#	0.22	0.18	0.20	0.38	0.17	0.16	0.27	0.30	0.27	0.26	0.18
FeO+MgO+Tio_2	4.95	5.69	5.08	4.42	4.51	4.17	4.09	5.24	3.80	3.51	2.84
FeO+MgO	4.31	5.34	5.05	4.37	3.60	3.94	3.95	5.11	3.70	3.47	2.67
K_2O/Na_2O	5.24	5.48	3.24	3.57	5.64	4.79	2.84	4.48	4.82	3.18	4.41

2.56	2.56
2.84	2.67
3.02	2.86
3.51	3.47
3.80	3.60
4.09	4
4.17	3.94
4.34	***3.95***
4.36	4.01
4.42	4.01
4.51	4.15
4.66	4.31
4.67	4.37
4.79	4.53
4.95	4.72
5.08	5.05
5.24	***5.11***
5.46	5.34
5.69	5.36

										Experiments		
32	35	34	3	6	36	39	21/22	**Aver.**	*Stdv*	P91	P91	KKB
24h	*24h*	*24h*	*24h*	*24h*	*24h*	*24h*	*4h*					n=11
1050	*1050*	*1050*	*1050*	*1050*	*1050*	*1050*	*1050*			*1025*	*1075*	*950*
1.7	*1.7*	*2.0*	*2.0*	*2.0*	*2.0*	*2.0*	*2.0*			*1.0*	*1.0*	*0.5*
70.97	70.92	68.83	71.07	68.24	71.97	71.91	66.36	**68.33**	(2.34)	70.62	69.44	73.96
0.22	0.15	0.13	0.10	0.00	0.33	0.66	0.07	**0.23**	(0.25)	0.65	0.73	0.11
13.18	14.00	12.06	11.83	13.46	13.23	11.93	13.14	**13.04**	(0.81)	13.4	13.64	12.95
3.53	2.41	3.97	4.75	2.22	3.49	3.47	3.54	**3.47**	(0.74)	3.26	3.04	3.03
0.06	0.09	0.01	0.01	0.00	0.03	0.08	0.07	**0.05**	(0.05)	0.11	0.08	0.04
0.62	0.45	0.56	0.61	0.34	0.52	0.54	1.18	**0.62**	(0.20)	1.04	1.09	0.65
1.09	0.58	0.54	0.60	0.98	0.56	0.84	0.88	**0.65**	(0.45)	0.26	0.28	0.53
2.11	2.17	2.29	2.45	3.03	2.68	0.96	1.52	**1.76**	(0.58)	0.79	0.84	1.10
5.81	6.68	6.18	6.07	6.69	6.51	6.45	6.13	**6.26**	(0.78)	5.98	6.05	6.72
0.17	0.07	0.07	0.00	0.12	0.25	0.20	0.38	**0.21**	(0.19)	0.11	0.06	0.03
0.00	0.01	0.09	0.10	0.10	0.10	0.00	0.01	**0.32**	(0.39)	-	-	-
97.76	97.53	94.64	97.49	99.07	99.57	97.05	93.29	**95.26**		96.22	95.25	99.12
31	29	27	27	25	27	37	29	**30**		39	37	37
2	2	1	0	0	1	2	3	**3**		5	5	3
34	39	37	36	41	38	38	36	**37**		35	36	40
18	18	19	21	25	23	8	13	**15**		7	7	9
4	2	2	3	3	1	3	2	**2**		1	1	2
8	5	8	10	4	7	7	9	**8**		8	7	7
1.12	1.18	1.05	1.01	0.95	1.06	1.18	1.22	**1.22**		1.63	1.62	1.29
2.24	2.47	5.36	2.51	0.93	0.43	2.95	6.72	**4.74**		3.78	4.75	0.88
0.24	0.24	0.20	0.19	0.21	0.21	0.21	0.37	**0.23**		0.35	0.38	0.27
4.36	3.02	4.66	5.46	2.56	4.34	4.67	4.79	**4.32**		4.95	4.86	3.79
4.15	2.86	4.53	5.36	2.56	4.01	4.01	4.72	**4.09**		**4.30**	**4.13**	**3.68**
2.76	3.07	2.69	2.48	2.21	2.43	6.71	4.04	**3.90**		7.57	7.20	6.09

Other Nanogranitoids

	BAR	*Stdv*	F16	*Stdv*	AV16	*Stdv*	AV07	*Stdv*	F11	*Stdv*	B13	*Stdv*
	n=4		n=4		n=5		n=62		n=15		n=15	
	830		*825*		*800*		*700*		*700*		*700*	
	0.8		*0.5*		*1.2/1.4*		*0.5*		*0.5*		*0.5*	
Stdv												
(2.63)	73.77	(2.34)	70.78	(3.44)	70.16	(1.29)	71.23	(1.43)	68.95	(1.65)	70.03	(2.28)
(0.09)	0.09	(0.08)	0.06	(0.05)	0.07	(0.06)	0.10	(0.03)	0.10	(0.12)	0.04	(0.07)
(1.31)	12.90	(1.46)	11.91	(0.68)	14.89	(0.98)	14.44	(0.33)	12.82	(1.14)	11.71	(0.86)
(0.69)	2.51	(0.37)	2.39	(0.76)	2.14	(0.59)	1.71	(0.52)	1.32	(0.40)	1.71	(0.21)
(0.03)	0.25	(0.17)	0.10	(0.10)	0.46	(0.07)	0.08	(0.05)	0.16	(0.17)	0.17	(0.10)
(0.21)	0.53	(0.13)	0.61	(0.07)	0.09	(0.02)	0.05	(0.04)	0.02	(0.03)	0.12	(0.07)
(0.20)	0.85	(0.48)	1.04	(0.56)	0.48	(0.13)	0.60	(0.09)	0.68	(0.16)	0.45	(0.13)
(0.32)	1.94	(0.13)	0.57	(0.45)	2.88	(1.24)	3.63	(0.39)	2.25	(0.35)	2.79	(0.35)
(0.70)	4.86	(0.79)	6.24	(1.10)	3.97	(1.00)	4.97	(0.31)	4.56	(0.83)	4.05	(0.39)
(0.05)	0.02	(0.02)	0.28	(0.09)	0.01	(0.01)	0.37	(0.09)	0.16	(0.07)	0.26	(0.23)
	-		-		-		-		-		-	
	97.73		93.97		95.15		97.16		91.02		91.33	
	39		39		35		29		36		36	
	3		3		5		3		3		3	
	29		37		23		29		27		24	
	16		5		24		31		19		24	
	4		3		2		1		2		1	
	6		6		5		3		3		4	
	1.29		1.24		1.50		1.16		1.30		1.19	
	2.27		6.03		4.85		2.84		8.98		8.67	
	0.26		0.30		0.06		0.04		0.03		0.10	
	3.13		3.05		2.30		1.86		1.44		1.87	
	3.04		**2.99**		**2.23**		**1.76**		**1.34**		**1.83**	
	2.51		11.01		1.38		1.37		2.02		1.45	

Garnet	Analysis	H_2O (wt.%)	*1σ error*	CO_2 (ppm)	*1σ error*	F (ppm)	*1σ error*
1	Exp4_M1_1	4.38	*0.05*	5073	*204*	6820	*106*
	Exp4_M4_1	5.24	*0.06*	4979	*201*	3198	*49*
2	Exp4_M2_1	4.83	*0.05*	538	*32*	1033	*15*
	Exp4_M3_1	5.00	*0.05*	790	*34*	7223	*112*
3	Exp3_MI_2	3.93	*0.05*	603	*34*	541	*8*
	Exp3_MI_6	4.09	*0.05*	3983	*164*	5462	*85*
4	Exp3_MI_3	4.46	*0.05*	8109	*339*	535	*8*
	Exp3_MI_1	1.64	*0.07*	113	*38*	79	*2*
	Exp3_tub_1	3.85	*0.05*	504	*32*	479	*7*
	Exp3_1	4.18	*0.17*				
	Exp3_2	4.29	*0.17*				
5	Exp3_3	3.84	*0.17*				
	Exp3_4	4.69	*0.17*				

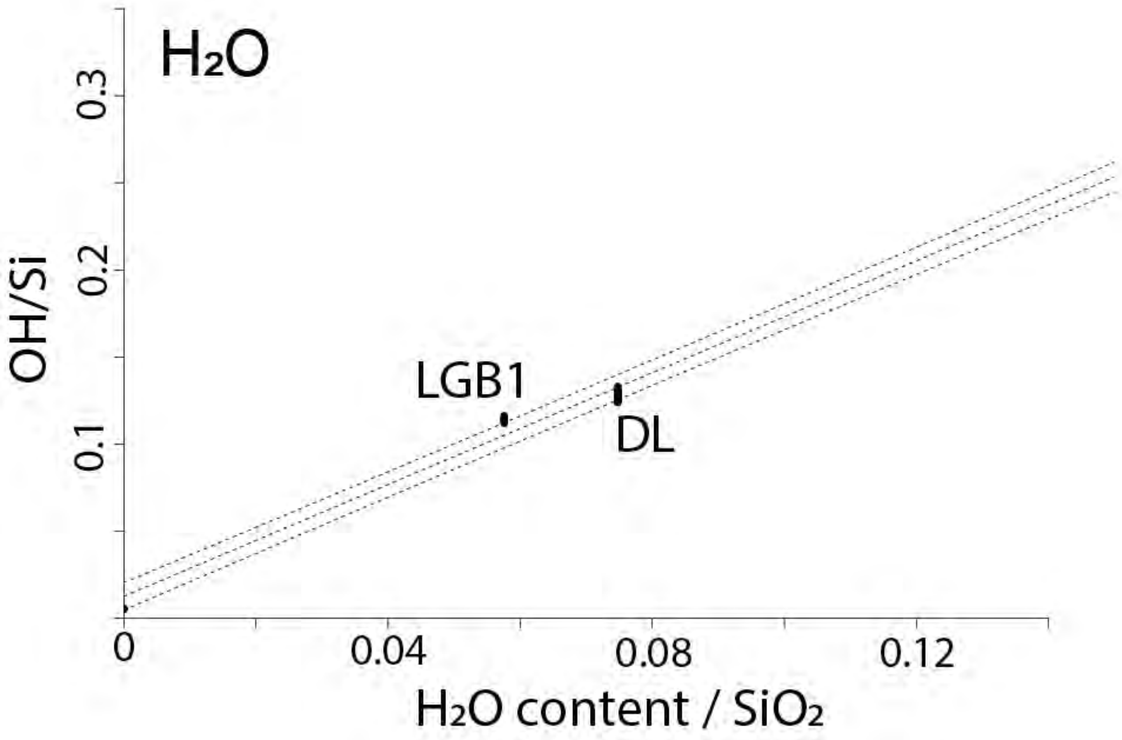
H₂O
OH/Si
0.3
0.2
0.1
LGB1
DL
0
0.04
0.08
0.12
H₂O content / SiO₂

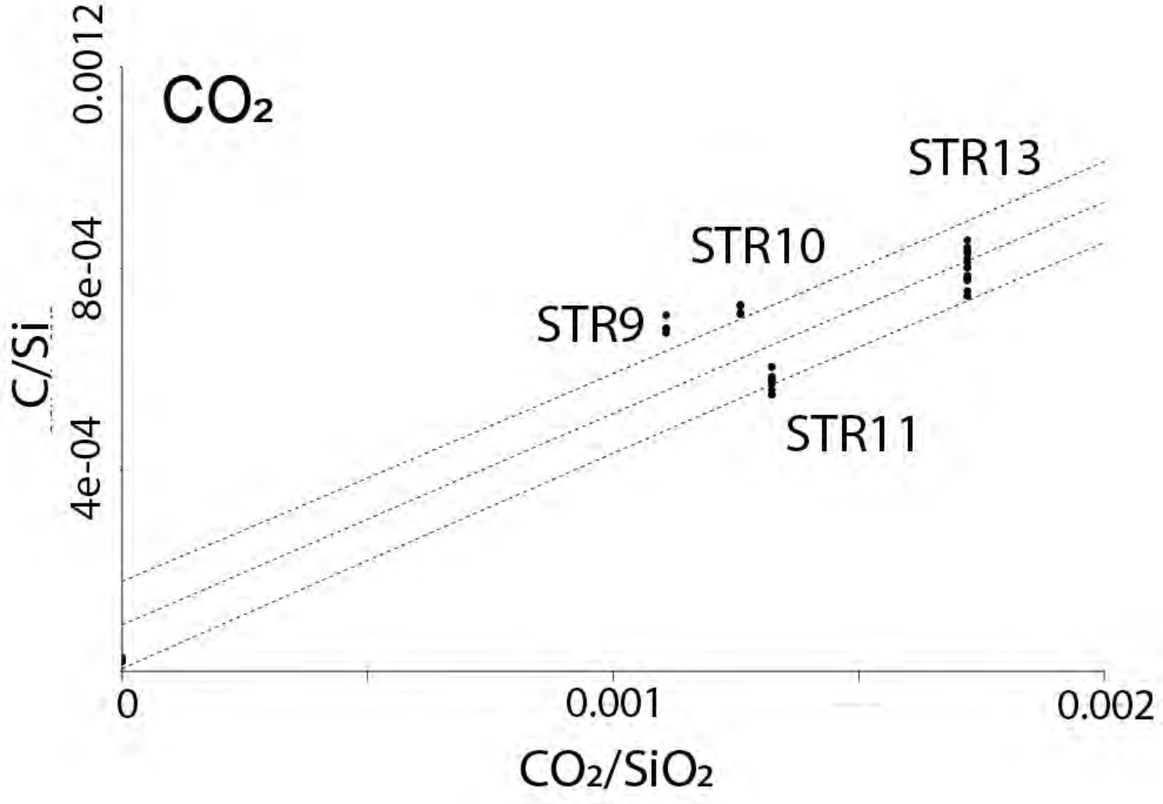
CO₂
C/Si
0.0012
8e-04
4e-04
STR13
STR10
STR9
STR11
0
0.001
0.002
CO₂/SiO₂

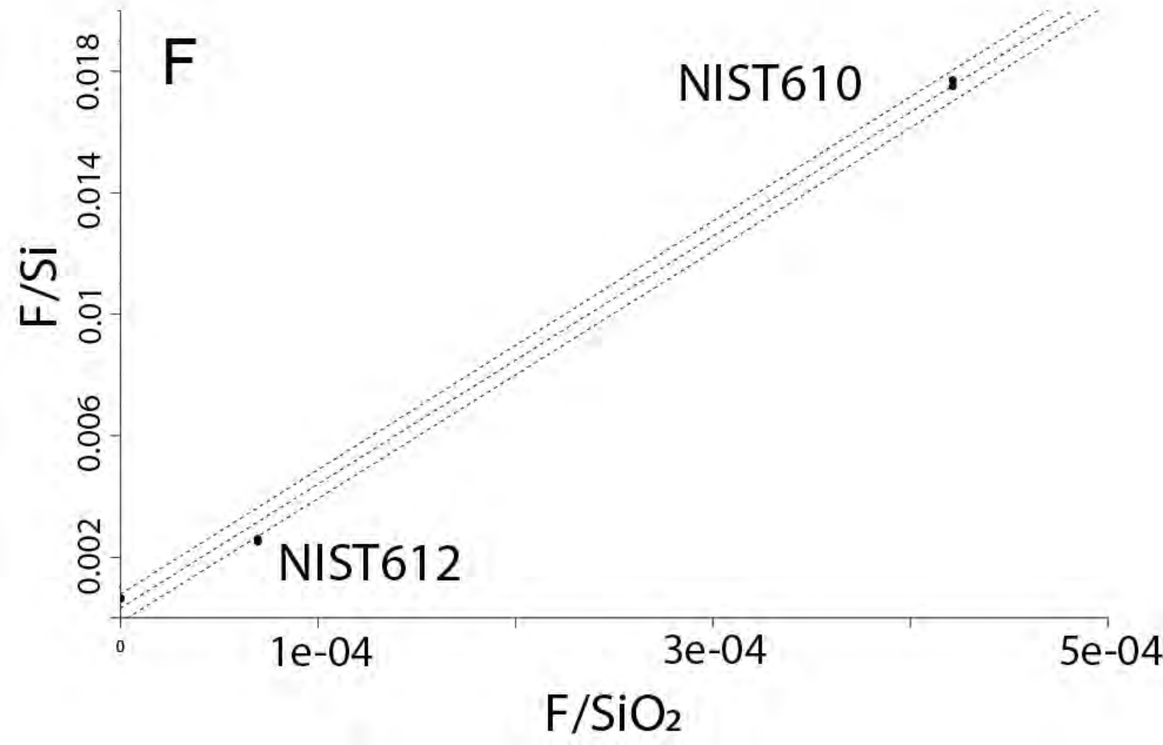
F
F/Si
0.018
0.014
0.01
0.006
0.002
NIST610
NIST612
0
1e-04
3e-04
5e-04
F/SiO₂

Name	**24**	**36**	**59**	**60**	**61**	**62**	**64**
Duration	*24h*	*24h*	*24h*	*24h*	*24h*	*24h*	*24h*
T (°C)	*1050*	*1050*	*1050*	*1050*	*1050*	*1050*	*1050*
P (GPa)	*1.0*	*1.0*	*1.2*	*1.2*	*1.2*	*1.2*	*1.2*
Wt%							
SiO_2	56.42	57.42	56.95	56.52	52.89	56.33	52.55
TiO_2	0.78	0.00	0.01	0.13	0.00	0.39	0.05
Al_2O_3	14.75	18.67	13.87	16.58	13.89	14.77	15.49
FeO	12.01	11.13	7.45	6.71	9.86	11.41	14.91
MnO	0.11	0.11	0.04	0.02	0.09	0.14	0.08
MgO	1.24	4.67	2.78	3.17	2.94	3.28	4.36
CaO	2.66	0.99	0.86	1.55	1.05	1.34	1.26
Na_2O	3.43	1.08	1.08	1.33	0.89	1.23	0.88
K_2O	3.48	4.20	4.98	5.75	5.03	3.10	3.47
P_2O_5	1.72	0.12	1.78	0.04	0.12	0.16	0.16
Cl	0.07	0.21	0.08	0.86	0.82	0.68	0.93
Total	96.49	98.65	89.74	91.78	86.67	92.00	93.13